Double Helicity Asymmetry for Charged Pion + Jet Production in p+p collisions at $\sqrt{s}$=200 GeV at STAR

ARCHIVES
MASSACHUSETTS INSTITUTE OF TECHNOLOGY
APR 26 2013
LIBRARIES

by

James Prewitt Hays-Wehle

B.S., Physics, Carnegie Mellon University (2006)

Submitted to the Department of Physics
in partial fulfillment of the requirements for the degree of

Doctor of Philosophy

at the

MASSACHUSETTS INSTITUTE OF TECHNOLOGY

February 2013

© Massachusetts Institute of Technology 2013. All rights reserved.

Author .....
Department of Physics
December 12, 2012

Certified by .....
Richard G. Milner
Professor of Physics; Director, Laboratory for Nuclear Science
Thesis Supervisor

Accepted by .....
John W. Belcher
Associate Department Head for Education

Double Helicity Asymmetry for Charged Pion + Jet Production in p+p collisions at $\sqrt{s}$=200 GeV at STAR

by

James Prewitt Hays-Wehle

Submitted to the Department of Physics
on January 25, 2013, in partial fulfillment of the
requirements for the degree of
Doctor of Philosophy

Abstract

Inclusive measurements from polarized proton-proton collisions at RHIC have constrained Δg, the polarized gluon distribution function of the proton. Correlation observables, such as this pion+jet measurement, allow for reconstruction of initial parton kinematics and are thus sensitive to the x dependence of Δg. By measuring charged pions opposite a jet, this particular measurement can be sensitive to the flavor of the struck parton. This measurement, which is dominated by the quark-gluon subprocess, can be divided into terms proportional to $\Delta u \Delta g$ and $\Delta d \Delta g$. The relatively larger quark polarization amplifies the measured asymmetry thereby enhancing the statistical power. This thesis presents the result of the mid-rapidity pion+jet longitudinal double spin asymmetry analysis from 10.6 pb^{-1} of luminosity collected in the 2009 200 GeV p+p run.

Thesis Supervisor: Richard G. Milner
Title: Professor of Physics; Director, Laboratory for Nuclear Science

Acknowledgments

I owe a great deal of thanks to many people without whom this work could never have been done.

Firstly, to my advisor Richard Milner, for guiding and supporting me through three different projects during my graduate studies.

To all the members of the RHIC-Spin group. I've had mentoring and guidance from Bernd Surrow and Joe Seele, but I've learned just as much from my fellow students Chris Jones, Matthew Walker, Michael Betancourt, Will Leight, and Ross Corliss, who all provided insight, expertise, and camaraderie.

Outside of the group, I value the friendships that I've had at MIT. Most notably Shawn, Parthi, Rachel, and Dan, but also many others.

I would never have made it to, or through, grad school if it were not for the love and support of my family.

Lastly and most importantly, to my fiancée Teesa, who has been with me through every step of this thesis and has been my greatest motivation to finish it.

THIS PAGE INTENTIONALLY LEFT BLANK

Contents

1 Introduction and Overview **15**

1.1 History 16

1.2 The Spin of the Proton 20

1.3 Measuring Gluon Polarization 22

1.3.1 Factorization 24

1.3.2 Fragmentation 26

1.4 The Analysis Channel 27

1.4.1 Pions 27

1.4.2 Jets 28

1.4.3 Charged Pion and Jet Correlations 28

2 Experimental Setup **31**

2.1 The Relativistic Heavy Ion Collider 31

2.1.1 Making Polarization 33

2.1.2 Maintaining Polarization 33

2.1.3 Measuring Polarization 34

2.2 The Solenoidal Tracker at RHIC 35

2.2.1 The Time Projection Chamber 36

2.2.2 The Barrel Electromagnetic Calorimeter 37

2.2.3 The Beam Beam Counters and Zero Degree Calorimeters . . . 37

3 Event Finding and Counting **39**

3.1 Event Structure 39

3.2 Triggering 40
3.3 Tracking and Vertexing 41
3.3.1 Jet-Finding 43
3.4 Pion Identification 43

4 A_{LL} Analysis **47**
4.1 Statistical Uncertainty 48
4.1.1 Multiplicity 48
4.2 Jet Energy 49
4.2.1 Jet Simulation 50
4.2.2 Jet Unfolding 50
4.3 Background Subtraction 55
4.4 Relative Luminosity 57
4.4.1 Accidental and Multiple Coincidence Corrections 58
4.4.2 Relative Luminosity Uncertainties 59
4.4.3 False Asymmetries 59
4.5 Polarization 61
4.5.1 Beam Transverse Component 62
4.6 Summary of Statistical Uncertainties 62
4.7 Summary of Systematic Uncertainties 63

5 Results and Conclusions **65**
5.1 Theory and Comparison 65
5.2 Agreement with Previous Results 67
5.3 Future Measurements 70

A Comparison of Data to Simulation **73**

B Additional Tables and Graphs **77**
B.1 Unfolding Matrices 77
B.2 Correlation of x and z with track p_T 79
B.3 Ratio of yields binned in z. 79

List of Figures

1-1 Diagram of a Deep Inelastic Scattering event. An electron carrying four-momentum k transfers a virtual photon with momentum $q = k - k'$ to a parton carrying a fraction x of the proton's momentum P. The inelastic final state particles are denoted as X. 17

1-2 World DIS data from both fixed target and collider experiments show Bjorken scaling: the invariance of the form factor F_2 with respect to Q^2.[4] At sufficiently low x the contributions of gluons and sea-quarks violate the scaling law, but this was not discovered until later experiments. 18

1-3 Gell-Mann's "Eightfold Way" shows $SU(3)$ flavor symmetry in baryons. This particular irreducible representation includes the Ω^-, a particle predicted by Gell-Mann's quark theory before it was discovered. [6] . 20

1-4 The EMC polarized DIS experiment probed into low x, where the measured quark polarization was not compatible with the Ellis-Jaffe predictions.[8] 22

1-5 Bounds placed on polarized PDFs, including $\Delta g(x)$. This is a global fit to both scaling violations in polarized Deep Inelastic Scattering and previous polarized proton measurements.[9] The yellow and green bands represent the $\Delta\chi^2 = 1$ and $\Delta\chi^2/\chi^2 = 2$ uncertainties, respectively. 23

1-6 Diagram of a hard scattering event in a proton-proton collision, labelled by important quantities. The diagram shows inclusive production of a hadron, h. This thesis measures events where h represents a charged pion. In the case of a π^+, there is a high probability that f_a and f_b represent a gluon and an up quark. 25

1-7 The dependence of subprocess fractions on p_T and z.[10] Quark+gluon dominates in this kinematic regime, but especially at high x and z. . 29

2-1 Schematic of RHIC accelerator complex. Protons start their journey at the Polarized H^- source before moving through the Linac, Booster, AGS and finally RHIC. 32

2-2 The STAR detector. Important subsystems, such as the Time Projection Chamber and Barrel Electromagnetic Calorimeter, are labeled. . 35

3-1 Jet+pion production in a proton-proton collision. Such an event often contains two jets in opposition and many pions within those jets. All charged pions are included in this analysis provided they are opposite a jet. 40

3-2 The likelihood of a vertex ranking for an example event.[25] 42

3-3 For a given momentum higher than MIP (such as the range indicated by the dashed red line), dE/dx corresponds to particle mass.[2] The momentum range where particles can be identified by this method is approximately 1-20 GeV/c. 45

4-1 Multiplicity of π^+ for each z bin (left) and x bin (right). Pions in a given event should frequently fall into the same x bin, but rarely into the same z bin. 49

4-2 The joint distribution of reconstructed jet p_T and true jet p_T. 51

4-3 An unfolding matrix and its effect: the unfolding matrix for π^+ binned in z (left) and the associated reconstructed (red) and unfolded (blue) distributions (right). 53

4-4 The unfolding matrix for π^- binned in x (left) and the associated reconstructed (red) and unfolded (blue) distributions (right). The diagonality of the matrix suggests the NLO approximation (Equation 1.10) is valid. 54

4-5 A simultaneous fit of distributions in $n\sigma_\pi$ for all particle species and both charges. 55

4-6 The single-spin false asymmetries as a function of run number. 60

4-7 The like- and unlike- sign false asymmetries as a function of run number. 61

4-8 Polarization by fill.[32] 62

5-1 The π^++jet A_{LL} as a function of z. 66

5-2 The π^-+jet A_{LL} as a function of z. The vertical black bars show the statistical uncertainties, while the green bars show the systematic uncertainties. 66

5-3 The π^-+jet and π^++jet A_{LL}s as a function of x. Note the agreement of the analysis using x_1, in red, to that using x_2, in blue. 67

5-4 The 2009 inclusive jet A_{LL}result[37] similarly suggests a ΔG larger than that predicted by DSSV, yet not as large as that used by GRSV-std. 68

5-5 The 2006 (blue) and 2009 (red) A_{LL}s as a function of z. The results agree well, especially at high z. 71

5-6 The combined A_{LL}s as a function of z. The combination smooths out the results at low z, but leave intact the high z conclusion that $A_{LL}$is higher than theory. 72

A-1 Spectra in x for positive pions in both data (red) and simulation including Geant (black). The lowest and two highest bins are not included in the A_{LL} analysis. 73

A-2 Spectra in x for positive pions in unfolded data (blue) and raw Pythia simulation (black). Again, the lowest and two highest bins are not included in the A_{LL} analysis. 74

A-3 Spectra in x for positive pions in data unfolded by the usual fashion (blue) and by a simulation sample initialized to flat (red) after only a dozen iterations. 75

B-1 Total track distribution in x and p_T. 79

B-2 Total track distribution in z and p_T. 80

B-3 The excess of positive pions compared to negative pions increases with z. 80

List of Tables

4.1 Values of $n\sigma_\pi$ used for particle identification. 56

4.2 Average polarization performance. 61

4.3 Statistics summary 63

4.4 Systematics summary 63

5.1 Final results for both charges and both binnings. 65

5.2 Confidence levels for the two leading theoretical models with respect to the z-binned results. 70

B.1 The unfolding matrix for π^+ binned in z. 77

B.2 The unfolding matrix for π^- binned in z. 77

B.3 The unfolding matrix for π^+ binned in x. 78

B.4 The unfolding matrix for π^- binned in x. 78

THIS PAGE INTENTIONALLY LEFT BLANK

Chapter 1

Introduction and Overview

The proton is one of the most important objects in all of science, and accounts for about half the mass of the visible universe. Though it has been almost a century since Ernest Rutherford discovered the proton in 1917, there are still things we do not understand about it. We now know the proton to be a composite object, a collection of quarks and gluons. One of the main questions of modern hadronic physics is exactly how these components come together to be a proton. Modern collider experiments are a valuable tool for probing the spin structure of the proton. This thesis deals with the specific issue of how the angular momenta of these constituents, specifically gluons, contribute to the spin of the proton. More than just solving an accounting problem about the proton's angular momentum budget, these measurements provide insight into how quarks and gluons, the fundamental particles of Quantum Chromodynamics (QCD), interact in a bound state.

This thesis presents a measurement of the double helicity asymmetry for events whose final state has a charged pion opposite a jet, produced in polarized proton-proton collisions at a center-of-mass energy of 200 GeV recorded during the 2009 run. The Relativistic Heavy Ion Collider (RHIC) at Brookhaven National Laboratory (BNL) is the only facility in the world able to collide polarized protons, and thus the only place this measurement can be done. This measurement was made by the Solenoidal Tracker At RHIC (STAR) experiment which recorded 14 pb^{-1} of integrated luminosity in 2009, almost twice the amount of any previous dataset. Thus, this

measurement will help further constrain knowledge of the gluon polarization in the proton.

The first chapter of this thesis presents the history and theory of the proton spin. The second chapter gives an overview of both the RHIC accelerator and the STAR detector. The third chapter details the measurement, and the fourth discusses the analysis and systematic errors. Finally, the fifth chapter concludes with the interpretation and implications of this measurement.

1.1 History

In 1933, Estermann, Frisch, and Stern[1] measured the magnetic dipole moment of the proton and found it 2.4 times greater[1] than expected for an elementary particle.[2] This was the first experimental clue to the compositeness of the proton, but it would be about 30 years until its constituents were discovered.

The next experimental breakthrough came from Deep Inelastic Scattering (DIS) experiments of the late 1960s. DIS refers to experiments where leptons (usually electrons) are scattered off a fixed target (usually containing protons) and interact electromagnetically with enough energy to disrupt the proton. See Figure 1-1 for an illustration.

Such an experiment at SLAC[3] in 1969[3] found that, at sufficiently high transferred momentum Q^2, the form factor of the proton no longer varied directly with Q^2. Q^2 is the square of the transferred four-momentum[4] and represents the length scale probed: the greater the momentum, the smaller the length. If the form factor does not change with Q^2, it follows that the proton looks the same on all length scales shorter than some critical value. This effect will only be observed if the proton is composed of free point-like particles, called at the time 'partons'. (In modern usage, 'parton'

[1]The current best measurement is $2.8\mu_N$.[2]

[2]The discrepancy is even clearer for the neutron, which has a magnetic dipole moment of $-1.9\mu_N$[2], while a fundamental neutral particle should have none at all.

[3]At the time, SLAC stood for Stanford Linear Accelerator Center. The laboratory is now the SLAC National Accelerator Center, with 'SLAC' no longer standing for anything.

[4]The four-momentum carried by the photon is q^μ. By the usual choice of metric signature, $q^2 < 0$, so we introduce the positive variable $Q^2 = -q^2$ for convenience.

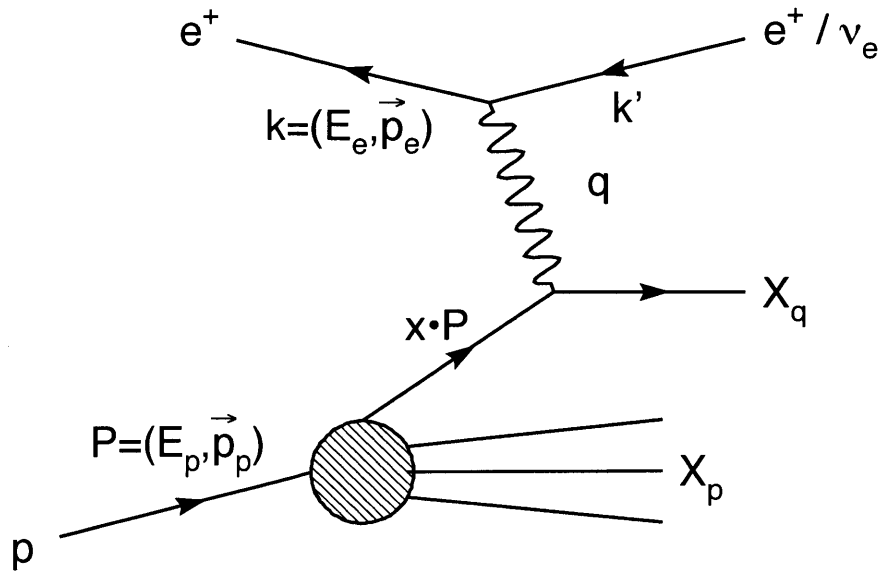

Figure 1-1: Diagram of a Deep Inelastic Scattering event. An electron carrying four-momentum k transfers a virtual photon with momentum $q = k - k'$ to a parton carrying a fraction x of the proton's momentum P. The inelastic final state particles are denoted as X.

denotes any constituent of the proton, be it quark, anti-quark, or gluon.) The effect is called the "Bjorken Scaling" law, after the theorist who predicted it based on the supposition that the proton was composed of point-like fermions (motivated by other results, discussed shortly).

As seen in Figure 1-2, the form factor of the proton depends exclusively on a single dimensionless ratio of the transferred momentum to the energy lost in the collision, known as the Bjorken scaling variable:

$$x = \frac{Q^2}{2M\nu} \tag{1.1}$$

where ν is the energy lost by the electron and M is the mass of the proton.[5] This variable is interpreted as the fraction of the proton's momentum carried by the struck parton, and will be used extensively in this thesis, most importantly in the description

[5] q and ν can be related by considering the invariant mass, W, of the hadronic system after collision. $W^2 = M^2 + 2M\nu + q^2$ means that when the proton remains intact, $W^2 = M^2$ gives $x = 1$, indicating the proton was addressed elastically as a whole. For a more complete treatment, see [5].

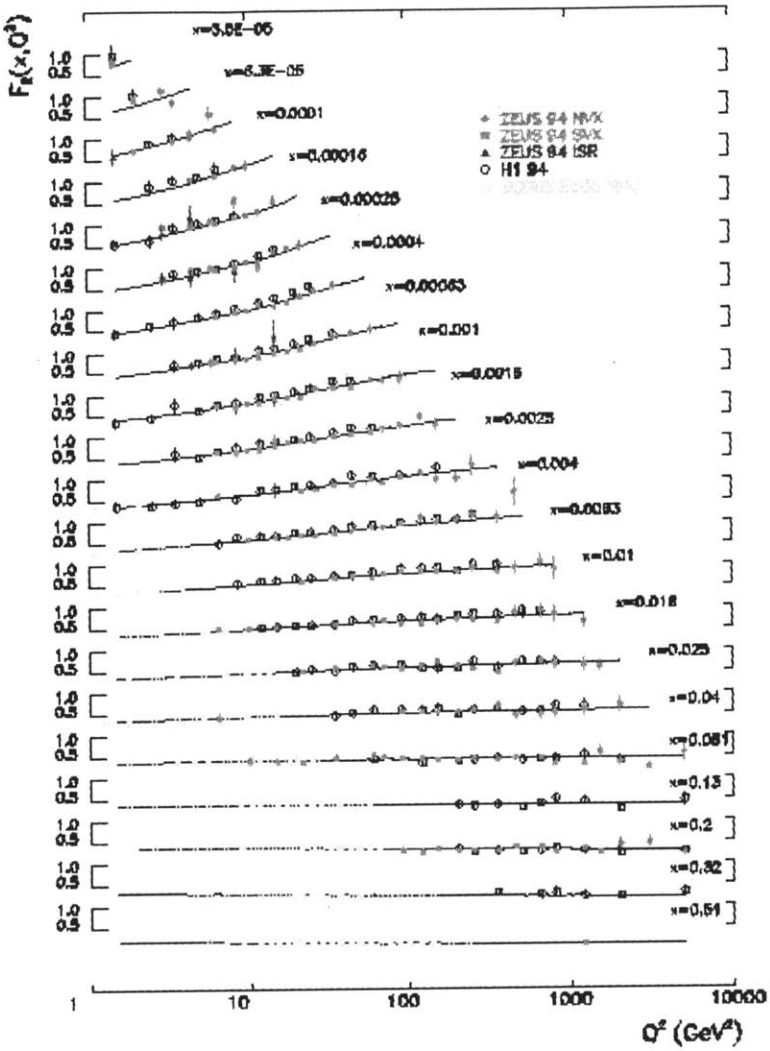

Figure 1-2: World DIS data from both fixed target and collider experiments show Bjorken scaling: the invariance of the form factor F_2 with respect to Q^2.[4] At sufficiently low x the contributions of gluons and sea-quarks violate the scaling law, but this was not discovered until later experiments.

of Parton Distribution Functions (PDF). A PDF, represented as $q(x)$ for quarks or $g(x)$ for gluons, gives the probability[6] that such a parton can be found within the proton carrying a momentum fraction x. This definition gives the convenient momentum sum rule that the fractional momenta of all partons should add up to the total momentum of the proton.

$$1 = \int_0^1 dx\ x\ (q(x) + \bar{q}(x) + g(x)) \tag{1.2}$$

The other major breakthrough for the quark-parton model came earlier in the 1960s. At the time, many experiments had discovered a large number of hadrons, affectionately referred to as the 'particle zoo,' and all initially believed to be fundamental. In 1964, Murray Gell-Mann grouped these particles by spin and organized them on axes of charge and strangeness. By this organization, he asserted that the proton and neutron were related to the other spin 1/2 baryons (the Σ and Ξ), in fact being the same save for some internal degree of freedom. This allowed him to posit that hadrons were composed of two or three fermions, which he called quarks. The quark model had its biggest vindication in 1964 with the discovery of the Ω^-, a particle Gell-Mann had predicted because it was missing from his decuplet of spin 3/2 baryons.[6]

The initial hesitance to identify partons with quarks was due to two main concerns: the seeming incompatibility of *free* partons being *bound* in a proton, and the continued non-observation of bare quarks. Both these concerns were addressed with the introduction of the theory of Quantum Chromodynamics (QCD). QCD is a fully relativistic quantum field theory which describes how quarks interact by the exchange of gluons. A striking feature of QCD, as compared to Quantum Electrodynamics (QED), is that the strength of the interaction increases with distance. Hence when quarks are bound together inside a proton, they experience almost no force, but the energy required to separate them is so large that it is energetically more favorable for the vacuum to create a quark+antiquark pair to bridge the gap. So at high Q^2 and

[6]PDFs are not normalized to be probabilities. instead they are normalized to the number of partons such that $\int_0^1 dx\ (q(x) - \bar{q}(x)) = 3$ reflects the three valence quarks.

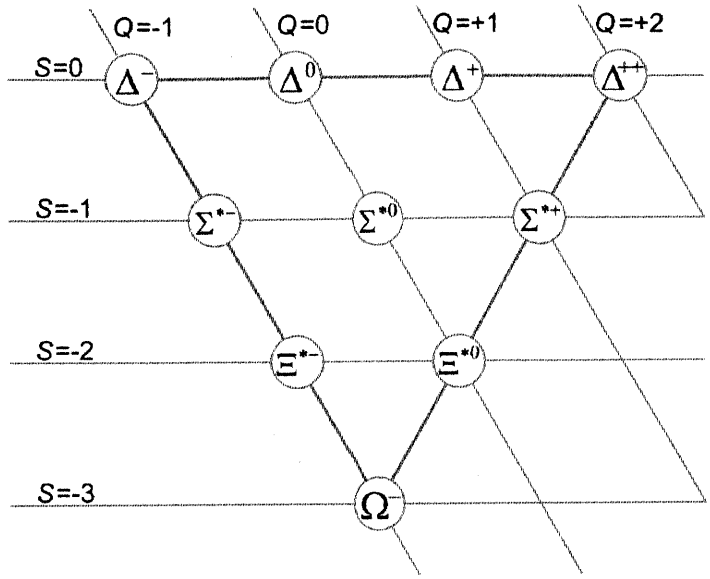

Figure 1-3: Gell-Mann's "Eightfold Way" shows $SU(3)$ flavor symmetry in baryons. This particular irreducible representation includes the Ω^-, a particle predicted by Gell-Mann's quark theory before it was discovered. [6]

short distances, quarks appear free, and at longer distances (lower Q^2), are bound in the proton. This effect is called "asymptotic freedom".

1.2 The Spin of the Proton

In the early static quark model of the proton's structure, the three quarks were all fully polarized, one pointing against the other two for a total of $\frac{1}{2}\hbar$.[7] This model was considered reasonably successful, as it could explain the spin, mass and magnetic moments of baryons. However, in the dynamic QCD picture, a static quark model is untenable because constant quark-gluon interaction means angular momentum is constantly being exchanged, and cannot be maintained by quark polarization at all times. Nevertheless, angular momentum must be conserved, and the spin of the proton must be a sum of the quark spin polarization, the gluon spin polarization, and their respective orbital angular momenta, represented as:

$$\frac{1}{2} = \frac{1}{2}\Delta\Sigma + \Delta G + \langle L_q \rangle + \langle L_g \rangle \tag{1.3}$$

[7] $\hbar = c = 1$ for the rest of this thesis.

where $\langle L_q \rangle$ and $\langle L_g \rangle$ are the average orbital angular momenta of the quark and gluon fields, respectively. $\Delta\Sigma$ and ΔG are the total quark and gluon polarization, respectively. The quark term gets a prefactor of 1/2 because that is the spin of a quark. Both polarization terms can be written in terms of PDFs. For example:

$$\Delta\Sigma = \sum_{q=u,d,s..} \int_0^1 dx(\Delta q(x) + \Delta\bar{q}(x)) \tag{1.4}$$

where Δq is the quark's polarized distribution,

$$\Delta q(x) \equiv q_+(x) - q_-(x) \tag{1.5}$$

and $q_{+(-)}(x)$ represents the probability of finding a quark with its spin aligned (anti-aligned) with the spin of the proton.[8] Likewise for the gluons:

$$\Delta G = \int_0^1 dx \Delta g(x) \tag{1.6}$$

Electromagnetic scattering experiments often express their results in terms of the spin-dependent structure function $g_1(x)$, which is weighted by the quark charges (+2/3 for up, −1/3 for down and strange).

$$g_1(x) = \sum_i e_i^2 \Delta q_i(x)$$

It is then possible to relate $\Delta\Sigma$ to $\int_0^1 dx\ g_1(x)$ using some simple assumptions.

In an unreasonable static quark picture, $\Delta\Sigma = 1$. But in light of fully interacting QCD, $\Delta\Sigma$ is guaranteed to be less than one. In 1974, Ellis and Jaffe predicted $\Delta\Sigma \approx 0.60$ based on beta decay data and $SU(3)$ flavor symmetry.[7] The first polarized DIS experiments at SLAC measured $g_1(x)$ through spin-dependent cross section asymmetry created by flipping the spin of both the target proton and probing electron. This measurement initially confirmed the Ellis-Jaffe prediction.

However, in 1987, the European Muon Collaboration (EMC) at CERN performed

[8]In the DIS formalism, the alignment is with respect to the direction of the virtual photon.

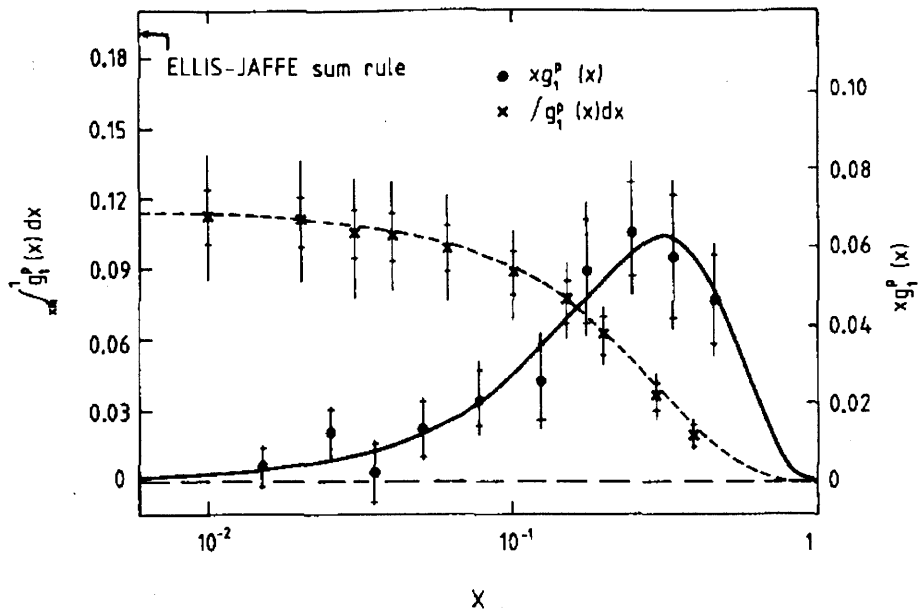

Figure 1-4: The EMC polarized DIS experiment probed into low x, where the measured quark polarization was not compatible with the Ellis-Jaffe predictions.[8]

a similar measurement, but probing much lower in x, and found that g_1 drops at low x. See figure 1-4. This meant that quarks carry only about 30% of the proton's spin.[8] This discovery was dubbed the "spin crisis," and began a line of inquiry into where the "missing" angular momentum could be found. The most promising candidate for holding some of the missing angular momentum (and the most feasible to measure) is the gluon polarization, ΔG.

1.3 Measuring Gluon Polarization

In polarized DIS, the spin polarization of gluons in the proton can be measured by scaling violations (variation with respect to Q^2) of $g_1(x)$. At low x, however, the available range of Q^2 shrinks, and measuring a trend over it is less reliable. Nevertheless, this technique has put bounds on the possible values of ΔG (see figure 1-5). However, because leptons do not interact with gluons, DIS measurement cannot directly access ΔG. For direct access to gluons, a hadronic probe is required. Of course, due to confinement, a beam of bare quarks or gluons simply cannot exist, but another spin polarized proton serves as a useful probe. A polarized proton collider

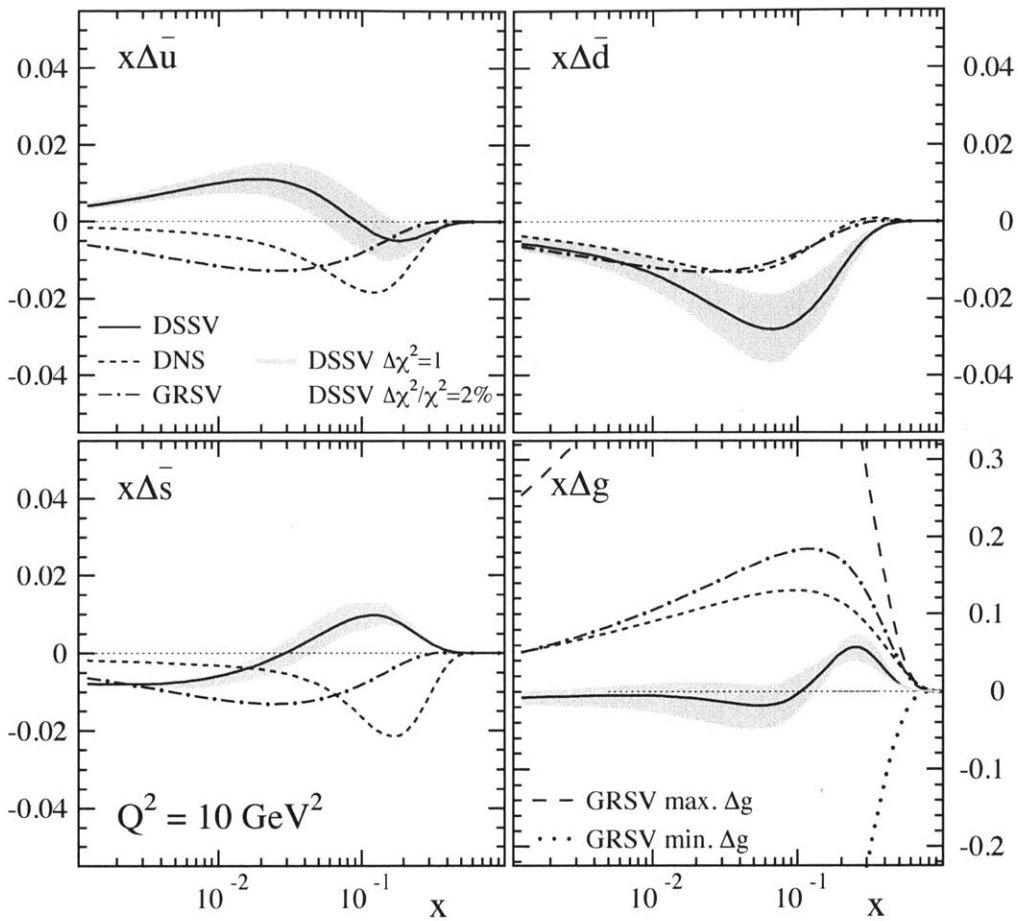

Figure 1-5: Bounds placed on polarized PDFs, including $\Delta g(x)$. This is a global fit to both scaling violations in polarized Deep Inelastic Scattering and previous polarized proton measurements.[9] The yellow and green bands represent the $\Delta\chi^2 = 1$ and $\Delta\chi^2/\chi^2 = 2$ uncertainties, respectively.

can measure the double longitudinal spin asymmetry, A_{LL}:

$$A_{LL} = \frac{\sigma^{++} - \sigma^{+-}}{\sigma^{++} + \sigma^{+-}} \tag{1.7}$$

which is the difference between a cross section for like-helicity collisions and the same cross section for unlike-helicity collisions, divided by their sum.[9] By choosing an

[9]We use a notation with two superscripts, one for each beam's helicity, and we actually measure A_{LL} using four total spin configurations. Because of parity conservation, $\sigma^{++} = \sigma^{--}$ and $\sigma^{+-} = \sigma^{-+}$. Ergo, an expression for A_{LL} using all four terms would be mathematically equivalent, however aesthetically inferior. See, for example, equation 4.2. A more careful treatment of beam polarizations and parity will appear in Section 4.4.3 on false asymmetries.

appropriate analysis channel, an A_{LL}measurement can directly constrain ΔG.

1.3.1 Factorization

QCD is notoriously difficult to calculate, especially at low energies where the coupling constant is largest. In this 'non-perturbative' regime, diagrams from all orders contribute on a somewhat equal basis. For this reason, theorists cannot simply calculate the properties of the proton from first principles and the boundary condition of having three net valence quarks. At high energies, the coupling constant drops and the situation resembles that of QED, where the lowest order diagrams dominate. In this 'perturbative' regime, theory can calculate cross-sections using only a few orders of diagrams.

Despite the simplification of the perturbative regime, a hadronic cross-section (either spin-dependent or independent) is a complicated physical object. But it can be made tractable by *factorizing* it into independent physical processes. The process by which two high energy protons collide to produce a hadron h, as shown in Figure 1-6, starts by selecting one parton from each proton, f_a and f_b. This selection of initial partons is determined by their PDFs, denoted $f_a(x_1)$ and $f_b(x_2)$, respectively. f_a and f_b then scatter into an intermediate parton f and anything else X, governed by the "hard scattering" differential cross section, $d\hat{\sigma}^{f_a f_b \to fX}$. This cross section is the tree level (two into two) parton scattering process only, and can thus be calculated with perturbative QCD. Finally, f can hadronize into the final state hadron, h. That last process is governed by a fragmentation function, $D_f^h(z, \mu^2)$.[10]

In the spin-dependent case, we must instead use a spin-dependent factorization. $\Delta\hat{\sigma}^{f_a f_b \to fX}$ is the spin-dependent component of the hard-scattering cross section, again calculable from perturbative QCD, and $\Delta f_a(x_1)$ and $\Delta f_b(x_2)$ are the polarized PDFs, as defined in Equation 1.5. Putting all these terms together, we have an expression for the A_{LL} of an inclusive production of a hadron, h, based on indepen-

[10]As with all QCD processes, fragmentation is formally dependent on a scale μ. This is not pertinent to the discussion, and is included only for completeness. This thesis uses theoretical predictions that take $\mu_F = \mu_R = (p_T^\pi + p_T^{jet})/2$ for both renormalization and fragmentation scales, and the sensitivity to this choice is discussed in [10].

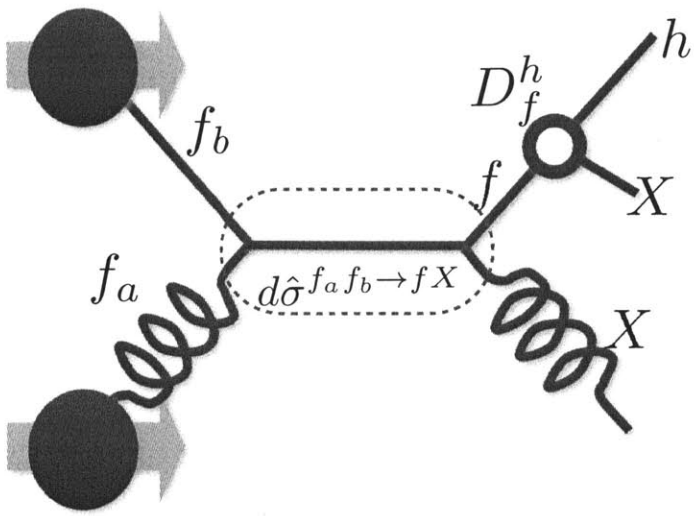

Figure 1-6: Diagram of a hard scattering event in a proton-proton collision, labelled by important quantities. The diagram shows inclusive production of a hadron, h. This thesis measures events where h represents a charged pion. In the case of a π^+, there is a high probability that f_a and f_b represent a gluon and an up quark.

dently calculable or measurable quantities:

$$A_{LL} = \frac{\sum_{f,f_a,f_b \in \{q,\bar{q},g\}} \Delta f_a \otimes \Delta f_b \otimes d\Delta\hat{\sigma}^{f_a f_b \to f X} \otimes D_f^h}{\sum_{f,f_a,f_b \in \{q,\bar{q},g\}} f_b \otimes f_b \otimes d\hat{\sigma}^{f_a f_b \to f X} \otimes D_f^h}$$

where $\otimes$ indicates a convolution, or an implicit integration over fractional momenta x_1, x_2, and z. The factorization formula is a sum over all initial parton collisions, $f_{a,b}$, which can be any combination of quarks, antiquarks or gluons. In particular, whenever f_a or f_b represents a gluon, the summed process is dependent on Δg. Thus, A_{LL} is a measurable quantity directly influenced by ΔG. The utility of the factorization formula comes from a notion of QCD *universality*: the theory that the PDFs, cross sections, and fragmentation functions are the same in every experiment. This means predictions for proton-proton collisions can be made by using historical data from seemingly unrelated DIS experiments, and much cleaner lepton collider experiments.

While this means $\Delta g(x)$ can be inferred from a measurement of A_{LL}, in practice it is done the other way: models based on data and assumptions about $\Delta g(x)$ make predictions for A_{LL}. This thesis will compare experimental results for A_{LL} to predictions made using two of the current leading models, DSSV[11] and GRSV-std[12].

These models are both phenomenological fits to existing world data, but there is still room for different predictions for $\Delta g(x)$ and other PDFs within existing constraints.

1.3.2 Fragmentation

A fundamental feature of QCD, as mentioned previously, is color confinement, the rule that a quark cannot exist for very long on its own. This phenomenon is a corollary to asymptotic freedom because as the interaction strength between quarks increases with separation, the space between them becomes so energetic that it is favorable to instead create a quark-antiquark pair between them. Depending on the energy of the parton, this can happen repeatedly, creating a large number of hadrons.

The process by which a quark becomes one or many hadrons is called *fragmentation* or *hadronization.* One important feature of the hadronization mechanism is that the initially separated quark loses only a part of its energy at each step, and so usually winds up in the hadron with the most momentum. If a single high momentum hadron is observed in the final state, then it surely carries one of the initially struck partons. If, on the other hand, many dozens of hadrons are observed all carrying similar momenta, it is impossible to tell where the initial parton wound up. To parameterize the spectrum between these two scenarios, the fragmentation fraction variable z is defined such that $z = 1$ indicates the hadron carrying the parton's momentum alone (and thus carrying the parton itself), and $z = 0$ indicates soft hadronic junk.

The fragmentation function $D_f^h(z, \mu^2)$ encodes the probability that the intermediate parton f will hadronize into a given hadron h carrying a fraction z of f's momentum. This prescription for fragmentation functions is similar to that used for PDFs, and likewise implies its own momentum sum rule:

$$1 = \sum_h \int_0^1 dz \; z D_f^h(z, \mu^2) \tag{1.8}$$

Like PDFs, fragmentation functions are not probabilities, but rather expected populations. An integration over momentum gives the mean number of hadrons produced by the parton: $\sum_h \int_0^1 dz D_f^h(z, \mu^2) >> 1$. Fragmentation functions can be measured

in cleaner e^+e^- collisions and DIS experiments.

1.4 The Analysis Channel

A_{LL} can be measured for any final state. The simplest case is "inclusive jets", i.e. any event with a jet (see 1.4.2). The measurement of that channel is a measurement of the relative rates of collisions that produce any hard scattering product that will hadronize. This thesis instead measures A_{LL} for a final state that includes a charged pion produced opposite a jet. The advantage in more exclusive ("semi-inclusive") observables, such as this jet-pion measurement or a dijet measurement, is that by reconstructing more of the final state, more information on the initial state can be recovered.

1.4.1 Pions

The pion is a meson, a bound state of a quark and anti-quark ($u\bar{d}$ for π^+ and $d\bar{u}$ for π^-). Charged pions have a mass of 139.6 GeV and, because they decay by the weak force, a lifetime of 2.6×10^{-8} seconds. By identifying pions in the final state, the identities of the initial state partons are better known. For example, a prominent positive pion in the final state probably came from a struck valence up quark. Thus, the A_{LL} for this process would be heavily dependent on $\Delta u \Delta g$, which puts a decent lever arm on Δg, as Δu is better known than any other polarized PDF.[11]

The same line of reasoning should also hold for inferring down quarks from negative pions. However, Δd is negative, so the prediction for the π^- A_{LL} is very different, as shown in the theory curves in Figure 5-2. Because fragmentation is a probabilistic process, it is never certain that a charged pion resulted from a particular quark. Yet the fragmentation functions and their z dependence can determine the probability with which it did. As z increases, we have an increase in "favored" fragmentation ($u \to \pi^+$ and $d \to \pi^-$) over "unfavored" fragmentation ($d \to \pi^+$ and $u \to \pi^-$).[11]

[11]This effect is also called "flavor tagging," though the term is more often applied to the identification of heavier quarks.

It should be noted that a neutral pion A_{LL} is also a useful measurement. The quark composition of the π^0, however, is $\frac{1}{\sqrt{2}}\left(|u\bar{u}\rangle - |d\bar{d}\rangle\right)$, equal parts up and down quark, meaning favored fragmentation does not apply. Furthermore, the π^0 decays rapidly to two photons, making measurement and detection completely different from the charged pion case. Therefore, neutral pions are considered separately. This thesis will use only charged pions. Please see [13] for the 2009 π^0 result.

1.4.2 Jets

When a high energy parton fragments into a large collection of particles, the collection is boosted into an energetic cone of hadronic particles, called a jet. Though they have no formal definition, jets are a clear signature of QCD fragmentation. They are useful to experimenters as a stand-in for an energetic parton because by conservation laws, the full energy and momentum of the quark or gluon should be that of the jet.

Jets were first observed in 1975 by the SPEAR experiment at SLAC, who noticed that hadron production in e^+e^- collisions was not azimuthally isotropic.[14] Previously, jets created at lower energy were too broad to be discernible as separate objects. Since that time, jets have been a powerful experimental tool. In 1978 PETRA recorded events with three jets (the signature of $e^+e^- \to q\bar{q}g$), which was the first direct observation of a gluon.[15] At the same time, the cross-section ratio,

$$R_{\text{Drell}} \equiv \frac{\sigma(e^+e^- \to q\bar{q})}{\sigma(e^+e^- \to \mu^+\mu^-)} = N_C \sum_f q_f^2$$

where N_C is the number of colors (3), was measured. This ratio increases in steps with center-of-mass energy, as heavier quarks become kinematically accessible, and was thus used to map out the masses of those quarks.

1.4.3 Charged Pion and Jet Correlations

In many previous analyses, A_{LL} was measured as a function of transverse momentum, p_T, the most obvious kinematic variable. (The experiment measures p_T directly (see

2.2.1) and, unlike η or $|\vec{p}|$, p_T is invariant with the boost of the collision.) However, the language of factorization uses the kinematic variables x for parton distributions and z for fragmentation, so an analysis making use of these variables could be of greater use in determining Δg. This analysis therefore focuses on the A_{LL} for a charged pion opposite a jet as a function of x or z. In order to use these kinematic variables, an away-side jet is required for better kinematic reconstruction.

As mentioned above, favored fragmentation increases with z. Additionally, in the kinematic region covered, z correlates with the portion of quark gluon scattering that makes up the cross section (as shown in Figure 1-7). Putting these effects together, the dependence of A_{LL} on $\Delta q \Delta g$ increases with z. On the other hand, all PDFs are functions of Bjorken x, so in order to better determine $\Delta g(x)$, it is helpful to measure the dependence of A_{LL} on x.

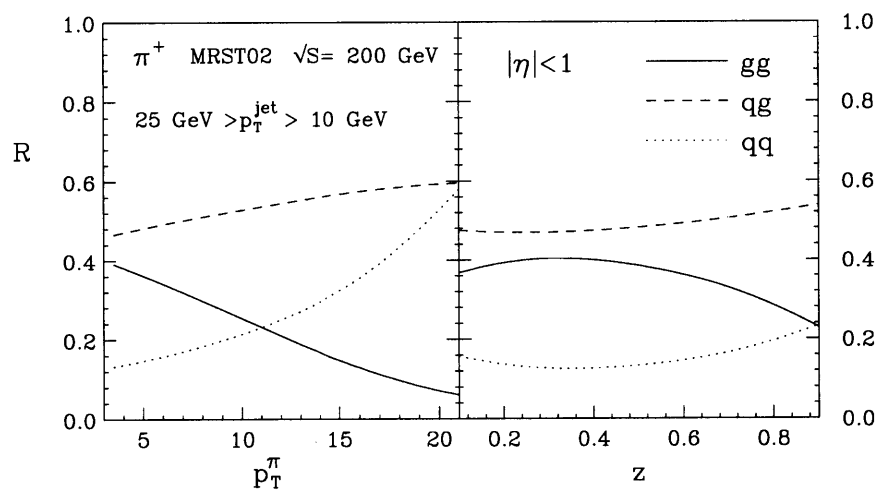

Figure 1-7: The dependence of subprocess fractions on p_T and z.[10] Quark+gluon dominates in this kinematic regime, but especially at high x and z.

Both of these variables, however, require measuring more than the pion. An away-side jet must also be measured. By asserting momentum conservation, it follows that the p_T of this jet should also be the p_T of the parton from which the pion fragmented. This gives an expression for fragmentation fraction.

$$z \equiv \frac{p_T^{\pi}}{p_T^{\text{jet}}} \tag{1.9}$$

Similarly, in order to measure x without complete reconstruction of the final state, a p_T balance must again be assumed. Also the pion is used to estimate the longitudinal direction of all hadrons on its side of the event.[12]

$$x_1 \equiv \frac{p_T^{\text{jet}}}{\sqrt{s}} \left(e^{\eta_{\text{jet}}} + e^{\eta_\pi}\right), \qquad x_2 \equiv \frac{p_T^{\text{jet}}}{\sqrt{s}} \left(e^{-\eta_{\text{jet}}} + e^{-\eta_\pi}\right) \tag{1.10}$$

where the directional quantity is pseudorapidity,

$$\eta \equiv -\ln\left[\tan\left(\frac{\theta}{2}\right)\right]$$

and $\sqrt{s}$ is the invariant mass of the proton+proton system, 200 GeV in this case. This definition is correct for Next to Leading Order (NLO) QCD. And its suitability at higher order is discussed in [10] and section 4.2.2.

Given these definitions, we set out to measure the A_{LL} for a charged pion opposite a jet, binned as a function of x or z.

[12]Phenomenologically, all of the hadrons on one side will cluster in a jet, motivating the approximation that they all have the same η. Theory arrives at the same conclusion from another direction: at leading order, only two partons are radiated, one of them becomes the pion which carries all of its momentum.

Chapter 2

Experimental Setup

In order to perform this measurement, one requires both an accelerator capable of delivering longitudinally polarized protons at energies in the realm of perturbative QCD and a detector able to measure all the products of these collisions with accuracy and certainty.

2.1 The Relativistic Heavy Ion Collider

Completed in 2000, the Relativistic Heavy Ion Collider (RHIC) is located at Brookhaven National Lab. In addition to its namesake work, measuring hot quark matter by colliding nuclei as heavy as gold, it is also the world's only facility for colliding polarized protons. It has achieved polarized proton collisions at center-of-mass energies as high as 500 GeV, To access polarized partons, however, lower energies are required for significant valence quark contribution[16]; so this measurement was carried out at an energy of 200 GeV.

In order to collide these polarized protons at the center of STAR and other experiments (known as interaction points), RHIC employs the lengthy accelerator complex depicted in Figure 2-1. H^- ions (protons carrying two electrons) leaving the polarized ion source (discussed later) are accelerated by a linear accelerator (LINAC) to 200 MeV. The protons are then stripped of their electrons. The now bare protons are accelerated by the Booster ring to 2 GeV before being injected into the Alter-

nating Gradient Synchrotron (AGS), where they are accelerated to 23 GeV. Once extracted from the AGS, the protons move through a switchyard, allowing them to be injected into RHIC in either direction, where they are accelerated to 100 GeV. The clockwise and counter-clockwise rotating beams in RHIC, known as the 'blue' and 'yellow' beams respectively, are filled separately. Each beam holds 110 bunches in 120 buckets. The empty buckets are an 'abort gap,' a space long enough to switch off a dipole to dump the beam if need be. The spin of one beam alternates with each bunch, and the other beam with every second bunch. The spin pattern is thereby fixed such that STAR samples all four pairings each four bunches. The beams are synchronized so that the same bunches from each beam collide with each other every time they pass through STAR. The spin configuration of a given bunch crossing is thus a simple function of its position relative to the abort gap.

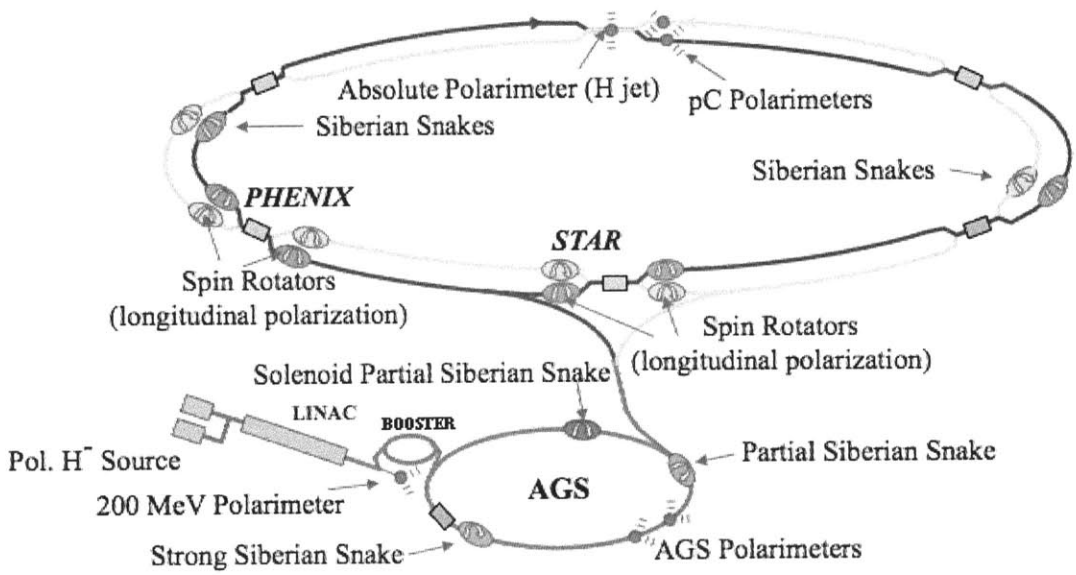

Figure 2-1: Schematic of RHIC accelerator complex. Protons start their journey at the Polarized H^- source before moving through the Linac, Booster, AGS and finally RHIC.

2.1.1 Making Polarization

In the Optically Pumped Polarized H^- Ion Source (OPPIS)[17], a low energy beam of protons is passed through a target of optically pumped rubidium vapor within a magnetic field. The Zeeman effect splits the energy levels of the rubidium's single valence electron into states which are aligned (or anti-aligned) with the magnetic field. The splitting energy is proportional to the magnetic field. The pumping laser is tuned to the transition from one of these states to a higher energy third state, which will decay back to one of the split ground states. By constantly vacating one of these polarization states, the other becomes completely populated. These electrons will then bond to the passing protons, which have a greater electron affinity than rubidium. Protons which do not pick up electrons are removed with an electrostatic field, and the remaining hydrogen atoms pass through a drift region where the magnetic field diabatically reverses. Known as the Sona transition, this process swaps the electronic and protonic spins in a $1^2S_{\frac{1}{2}}$ hydrogen atom[18] so the proton becomes polarized. Once the proton is polarized the neutral atoms pass through a sodium vapor and acquire one more electron. The H^- ions are accelerated through a LINAC before passing through a foil to strip off both electrons. The polarized protons are then accelerated by a small booster ring, then by the AGS, and are then finally injected into RHIC.

2.1.2 Maintaining Polarization

In both RHIC and the AGS, polarized protons are stored with their spins vertically aligned. If these machines had only pure dipole fields, the spins would precess uniformly about the dipole field. If oriented with the field, the spins would remain stationary. In a real synchrotron, there are both focussing fields and stray non-vertical fields (due to misalignment), which change the axis and frequency of precession, and lead to depolarization. To mitigate this, a pair of Siberian Snakes[19] flip the spin by 180° each turn so that any precession error accumulated in one lap is undone in the next. In order to convert these transversely polarized protons into longitudinally

polarized protons at the interaction points, special magnets positioned on either side of the experiment rotate the protons to longitudinal and then back to vertical on the other side of the experiment.

2.1.3 Measuring Polarization

The polarizations of both beams must be measured and monitored. The polarization measurement is vital because the asymmetries measured are directly scaled by the beam polarization. It is also important to monitor how the polarization degrades with time, not only for properly averaging it over a fill, but also as a diagnostic tool to ensure the storage ring maintains polarization. At RHIC this is accomplished with the use of five Coulomb-Nuclear Interference (CNI) polarimeters[20]. The CNI polarimeter is a thin carbon strip which can be moved in and out of the beam path. The collisions between the protons and this strip are mediated by a Coulomb (spin-dependent) interaction and a hadronic (spin-independent) interaction. At low momentum transfer, these two effects interfere and cause a left-right asymmetry. Thus, an asymmetry in the yield of recoiling carbon nuclei to either side of the strip is used to determine the proton beam polarization. The accelerator complex has five such CNI polarimeters: two for each beam in RHIC, and one positioned between the LINAC and the AGS booster to measure the source polarization. The analyzing power, or intrinsic asymmetry, of the CNI polarimeter is not known a priori. A second polarimeter, the Hydrogen Jet polarimeter, is used to calibrate it. The H-Jet has a much lower yield, so cannot be used alone, as it would never accumulate enough data to measure the polarization accurately. The H-Jet works on exactly the same physical principle, but because the hydrogen gas target is free, the collision products are not subject to multiple scattering as in the carbon solid, and so the kinematic relations are exact.

2.2 The Solenoidal Tracker at RHIC

The above describes how RHIC produces polarized proton collisions. Measuring the results of those collisions is a parallel challenge. The Solenoidal Tracker at RHIC (STAR) is one of two general-purpose particle physics detectors running at RHIC, the other being PHENIX. As the name implies, the centerpiece of the experiment is a large tracker – a Time Projection Chamber (TPC) – in a half Tesla solenoidal magnetic field. The experiment is located at the 6 o'clock position on the southern edge of RHIC, in between the blue and yellow injection lines (see figure 2-1). In addition to the TPC, the suite of detector subsystems includes electromagnetic calorimetry, time-of-flight detectors, dedicated luminosity and triggering detectors, and a host of others not used for this measurement.

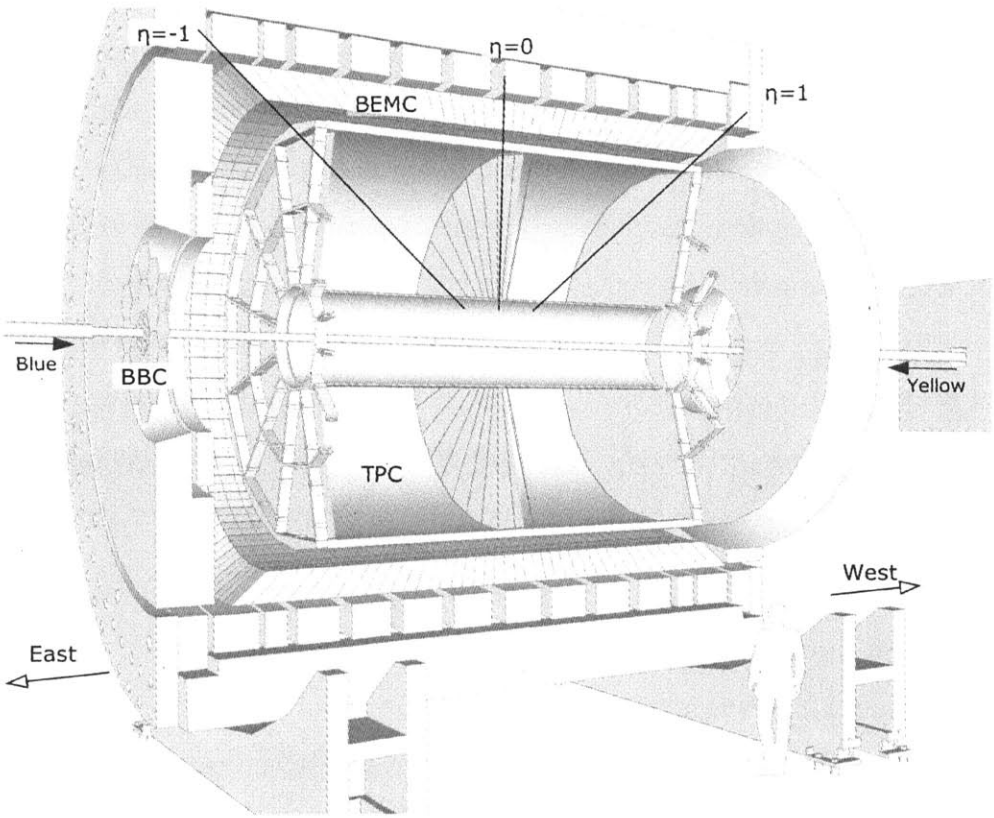

Figure 2-2: The STAR detector. Important subsystems, such as the Time Projection Chamber and Barrel Electromagnetic Calorimeter, are labeled.

2.2.1 The Time Projection Chamber

A Time Projection Chamber (TPC) is a gas tracking volume with an electric field which defines the drift direction. Charged particles that pass through the TPC ionize the gas, and the ionization track drifts to a readout plane at either end of the chamber. By measuring the time that the ionized electrons arrive at the readout plane, a TPC can also reconstruct the track's distance from and inclination to the plane. If the tracking volume is placed inside a magnetic field, then the track's curvature gives the momentum transverse to the magnetic field. In either a solenoidal or toroidal field, this momentum is p_T, the momentum transverse to the beam direction. Aligning the drift direction with the magnetic field allows for the best reconstruction of a track's curvature (and thus p_T) and furthermore avoids complications arising from $E \times B$ drift. Additionally, the strength of the ionization, dE/dx, can be used to identify the type of particle. The TPC[21] at STAR is a 4.2 m long by 4 m diameter cylinder of P10 gas (90% argon, 10% methane) inside a 0.5 Tesla solenoidal magnetic field. It is divided in half by a central membrane, which is held at 28 kV. The membrane, together with a peripheral field cage, creates a uniform electric field of 135 V/m, which causes the ionized electrons to drift towards the outside ends of the cylinder at a velocity of approximately 5.45 cm/μs. The electrons are absorbed by a 'gating grid' of alternately biased wires. When the TPC is read out, the gating grid is shut off, and the electrons are allowed through into an amplification region, where they shower and are measured by an array of Multiwire Proportional Chambers.

Because the ionization must drift up to two meters, it takes longer to read out the TPC than the time in between bunch crossings. This means, firstly, that the TPC is not fast enough to determine whether an event is worth recording. A much faster calorimeter is instead used for triggering (see below for the calorimeter and 3.2 for triggering). Secondly, the tracks from many different events will be piled-up in the same TPC readout, so determination of which tracks are relevant (and not artifacts from previous events) requires auxiliary timing information. (See 3.3 for tracking and vertexing).

2.2.2 The Barrel Electromagnetic Calorimeter

The Barrel Electromagnetic Calorimeter (BEMC)[22] is situated directly outside the TPC, covering its entire outside surface, -1 to 1 in pseudorapidity and 2π in azimuth. It is a sampling calorimeter made of 21 layers of plastic scintillator interleaved with layers of lead each 1 cm thick. The BEMC is divided into 4800 towers, each subtending 0.05 x 0.05 in $\eta \times \phi$. All the scintillator layers in one tower are read out by wavelength shifting fiber to the tower's photomultiplier tube. The two main duties that the BEMC will serve in this thesis are jet measurement and triggering. The BEMC provides triggering because the TPC takes much more time to read out.

2.2.3 The Beam Beam Counters and Zero Degree Calorimeters

The Beam Beam Counters[23](BBCs) and Zero Degree Calorimeters[24](ZDC)s are both used as dedicated luminosity monitors. The BBCs are two sets of hexagonally tiled scintillators placed in a ring about the beam axis, 3.7 meters on either side of the interaction point and subtending the pseudorapidity $3.3 < |\eta| < 5$. Energy deposited in this area usually comes from forward hadronic jets, which occur more frequently than mid-rapidity jets, yet indicate the same underlying physics. The increased rate gives this process better statistical resolution of the luminosity. Similarly, events which see both East and West BBCs hit indicate a dijet event.

The ZDCs are a pair of tungsten sampling calorimeters placed outside the last bending magnets in RHIC which split the yellow and blue beams. In this way, it is designed to measure neutrons emitted within 4 mrad of the beam axis. Neutrons from forward diffractive processes are produced by an up quark being struck from the proton and replaced by a down quark from the vacuum. Because these neutrons are mostly the original protons, they are a very linear measure of luminosity.

Because of their different acceptances and particle sensitivities, the ZDCs and BBCs sample very different processes at very different rates, and so should provide largely independent measurements of luminosity

THIS PAGE INTENTIONALLY LEFT BLANK

Chapter 3

Event Finding and Counting

3.1 Event Structure

This thesis deals with a very particular final state of proton+proton collisions: events that have a charged pion opposite a jet. Charged pions carry flavor information from the proton. Observing them opposite a jet ensures that both fragmented from the same hard hadronic collision. "Opposite" is experimentally defined as a separation between the pion track and the jet cone axis of 2 radians in azimuth, $|\Delta\phi| > 2.0$. The pions must have a transverse momentum of 2 GeV/c $< p_T <$ 13 GeV/c , while the jet must have 10 GeV/c $< p_T <$ 30 GeV/c Both jet and pion must be "in the barrel," having a midrapidity range $|\eta| < 1$.

While this phase space may seem overly specific, DeFlorian notes the predicted asymmetry is "almost insensitive to the precise value of those cuts."[10] All other cuts are made to ensure a correctly reconstructed event. Most notably, pion candidate tracks must be reconstructed from at least 20 points in the TPC. To ensure the pion and jet came from the same collision, another cut requires both be 2 cm or closer to the primary vertex. (See Section 3.3 for details)

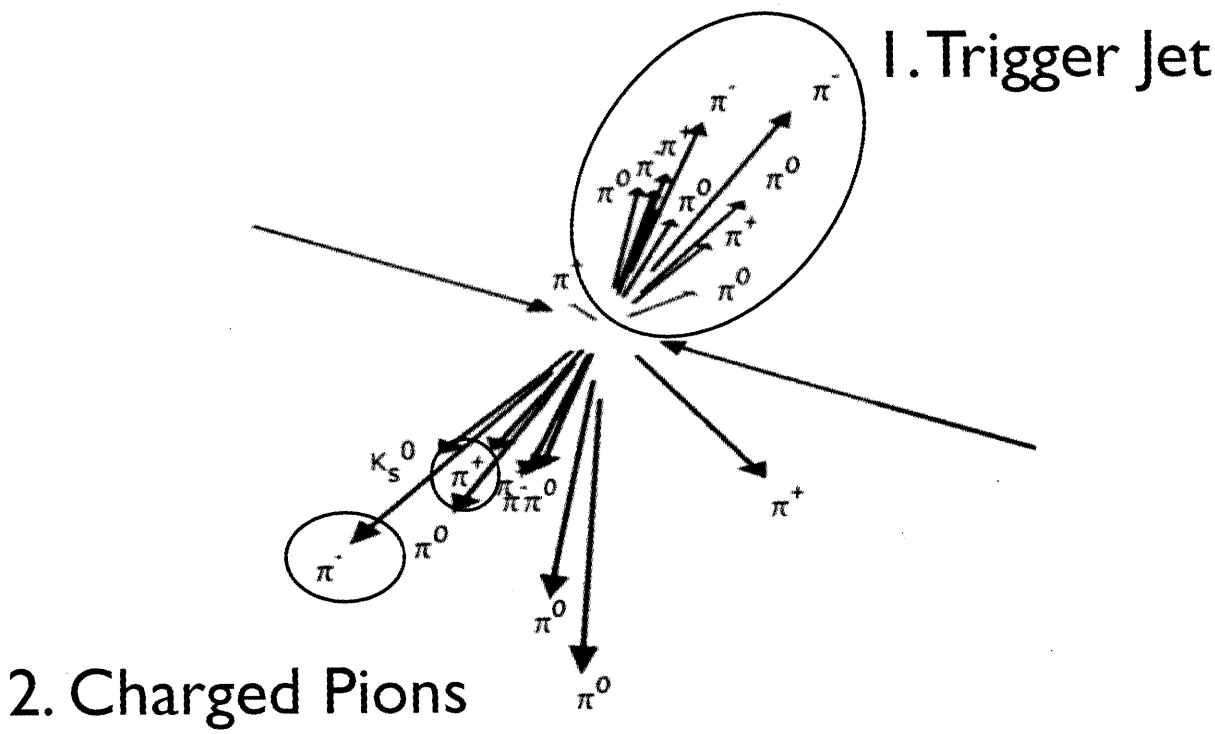

Figure 3-1: Jet+pion production in a proton-proton collision. Such an event often contains two jets in opposition and many pions within those jets. All charged pions are included in this analysis provided they are opposite a jet.

3.2 Triggering

An event begins when one of many triggers determines some criteria has been met that indicating the event is worth recording. Because the TPC takes considerable time to read out, STAR relies on signals from detectors other than the TPC. The simplest of these is the Minimum Bias (MB) trigger, which fires on a East and West coincidence in the BBC. On top of that, this analysis uses the following BEMC based triggers:

- Barrel Jet Patch 1 (BJP1): Triggered if one of twelve fixed 1x1 patches in $\eta \times \phi$ receives more than 5.4 GeV of transverse energy.

- Level 2 Jet High (L2J): Triggered if any 1x1 patch in $\eta \times \phi$ receives more than 6.5 GeV of transverse energy.

The BEMC is sensitive only to electromagnetic energy, so a jet can have more total energy than the trigger requires yet not enough electromagnetic energy to satisfy the trigger requirements. Specifically, the calorimeter responds differently to hadrons than to photons at the same given momentum, meaning that the particulars of fragmentation could determine the amount of energy deposited in the calorimeter. A cut requiring jets with $p_T > 10$ GeV/c ensures all the events chosen are sufficiently well-above the trigger threshold. This cut removes sensitivity to jet energy at the trigger threshold which can, in certain cases, introduce a bias.

3.3 Tracking and Vertexing

Once an event has been triggered, the TPC is read out, and the charged particle tracks it measured are determined. Several non-triggering collisions can occur in the bunch crossings before an event causes the TPC to read out. When the TPC is triggered, the ionized tracks from these previous events may still be drifting through the gas volume. Furthermore, each event often contains several tracks, which require careful sorting on their own. The high occupancy in the TPC produces a few challenges for reconstructing tracks and vertices; careful algorithms are used to ensure the correct association of hits with tracks and tracks with vertices.

STAR uses a Kalman filter approach to turn a series of hits in the TPC into a track. Track seeds are usually started at the outer edge of the TPC, where the density of hits is lowest. The seed is a collection of only a few hits, sufficient to form an initial estimate of the track's helix. The Kalman filter then iteratively adds the seed track the best fitting hit point: the point causing the least $\Delta\chi^2$ to the track fit. The filter then recomputes the best fit track for the extended collection of points. The tracks are continued until either they reach the inner radius of the TPC, or no suitable hit points are found.

Matching tracks to calorimeter hits is also important for vertexing, because the

matched tower hit implies the track was caused by the current (triggered) event, and not a piled-up track from a previous collision. In the case of a pile-up track, the tower clears, and the track drifts away. The Pile-up Proof Vertexer (PPV)[25] weights tracks by whether they have matching towers and whether they are continuous across the central membrane, as an out-of-time track crossing the central membrane would be split as the tracks on either side drifted outwards. Tracks are extrapolated back to the beamline, and their point of closest approach to the beamline is evaluated. These potential track vertices are grouped into clusters of up to 3 cm long along the beamline. These clusters are scored with the sum of the weights of their tracks and then the clusters are ranked by these scores and the vertex with the highest rank is referred to as the 'primary' vertex. 'Primary' tracks, the only ones used in this analysis, are then the tracks which point to the primary vertex.

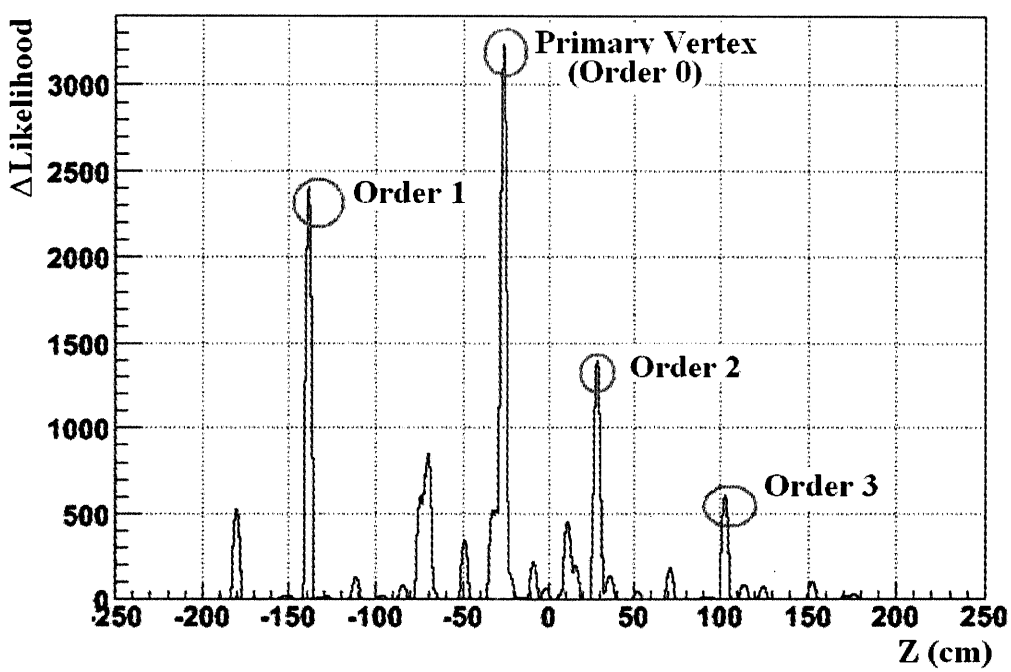

Figure 3-2: The likelihood of a vertex ranking for an example event.[25]

A minimization of each primary track's Distance of Closest Approach (DCA) to the primary vertex finds the most likely location of the vertex both along the beam direction and in the transverse dimensions.

Because the jet-finding algorithm is seeded on calorimeter hits and not the TPC,

the jet is guaranteed to be in-time, and its tracks will overwhelmingly determine the primary vertex. A requirement for the tracks of pion candidates to pass within 2 cm of the primary vertex becomes sufficient to guarantee the pion and jet come from the same collision.

3.3.1 Jet-Finding

Once the trigger declares there should be a jet in the event, and the TPC resolves all the tracks in the event, and the PPV has found a positive ranking vertex, then a jet-finding algorithm must determine how many jets there are, where they are, and what energies they have. Jets are found with a 'mid-point cone' algorithm[26], which is an iterative process that selects tower energies from the BEMC and associates them with clusters if they are within a specified radius,

$$\Delta R = \sqrt{(\Delta\eta)^2 + (\Delta\phi)^2} \leq 0.7 \tag{3.1}$$

of the energy-weighted center of that cluster. The algorithm starts with 'seeds' of any tower above 500 MeV and adds to them towers with at least 100 MeV within their local cone radius. The result is a collection of 'proto-jets,' based on the highest energy towers. The algorithm adds smaller towers incrementally, recomputing the center of the jet-cone after each, until a stable configuration is achieved. Jet cones may overlap, so jet pairs sharing more than 50% of their energy are merged into a single jet, while jets sharing less than 50% are split into separate jets. The momentum of the jet is the sum of the momenta of all its constituent proto-jets.

3.4 Pion Identification

Charged pions decay by the weak force, and so live long enough to exit the TPC, leaving a track of ionization. Identifying tracks as resulting from charged pions is based almost entirely upon the energy per distance deposited in the TPC, dE/dx. For a given momentum in the relativistic rise section of the Bethe-Bloch function, (see

Figure 3-3) dE/dx depends on the mass of the particle, and accordingly the species. The individual particle spectra diverge for a certain momentum range, approximately 1-20 GeV/c. This momentum range of species separation bounds the range in which pions can be feasibly identified.

The expectation value and variance of dE/dx are both functions of momentum, carrying the somewhat unwieldy units keV/cm. For convenience, we introduce the dimensionless variable $n\sigma_\pi$, which is simply dE/dx adjusted and rescaled to the expectation value and variance of dE/dx of a pion with the same momentum. By this convention, a track's $n\sigma_\pi$ is a measure of how many standard deviations its dE/dx is from the pion mean, such that a distribution of only pions in $n\sigma_\pi$ should have a mean of zero and a standard deviation of one. A p_T dependent cut is made in $n\sigma_\pi$ around the central pion peak. The location and determination of this cut are discussed in Section 4.3.

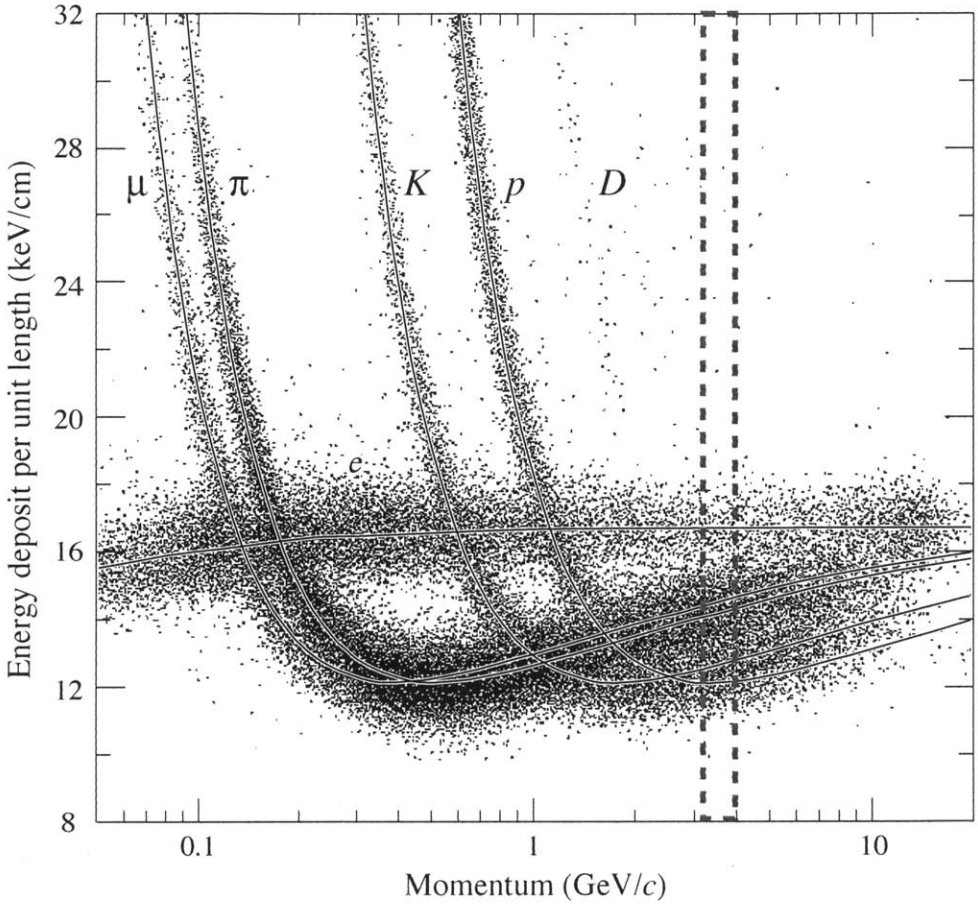

Figure 3-3: For a given momentum higher than MIP (such as the range indicated by the dashed red line), dE/dx corresponds to particle mass.[2] The momentum range where particles can be identified by this method is approximately 1-20 GeV/c.

THIS PAGE INTENTIONALLY LEFT BLANK

Chapter 4

A_{LL} Analysis

In Chapter 1, the double-longitudinal spin asymmetry, A_{LL}, was defined as:

$$A_{LL} = \frac{\sigma^{++} - \sigma^{+-}}{\sigma^{++} + \sigma^{+-}}$$

Each cross section is a physical observable pertaining only to the given spin configuration. This observable corresponds to an independent measurement from two purely polarized beams with well-measured luminosities. Any actual measured asymmetry is diluted by imperfect polarization, and this must be accounted for. One advantage of measuring an asymmetry, as opposed to a cross section, is the ratio's invariance to overall luminosity and efficiencies, which should both be spin independent. The asymmetry is expressed in experimental terms as

$$A_{LL} = \frac{1}{P_Y P_B} \frac{N^{++} - RN^{+-}}{N^{++} + RN^{+-}}, \tag{4.1}$$

where P_Y and P_B are the polarizations of the Yellow and Blue beams, respectively. R is the relative luminosity, a measured ratio of the luminosities of different types of bunch crossings,

$$R = \frac{L^{++}}{L^{+-}},$$

which is fairly close to unity. Finally, $N^{++(+-)}$ are the raw yields of events for even(odd) sign collisions. So the measurement can be reduced to event counting,

along with measurements of polarization and relative luminosity.

Polarization was measured on a per fill basis, where a fill is the period between beam injection and dump. Relative luminosity was measured in terms of 'runs,' with a run being a data-collecting interval of roughly an hour. To add all the yields from all the runs together, we express A_{LL}as:

$$A_{LL} = \frac{\sum_{i\in\text{runs}} P_{Y,i}P_{B,i}(N_i^{++} + N_i^{--} - R_i(N_i^{+-} + N_i^{-+}))}{\sum_{i\in\text{runs}} P_{Y,i}^2 P_{B,i}^2(N_i^{++} + N_i^{--} + R_i(N_i^{+-} + N_i^{-+}))} \tag{4.2}$$

4.1 Statistical Uncertainty

The uncertainty on A_{LL} due to the uncertainty in the yields N^{++} and N^{+-} is

$$\sigma_{A_{LL}}^2 = \frac{4}{P_Y^2 P_B^2 \left(N^{++} + RN^{+-}\right)^4} \left(\left(\sigma_{N^{+-}} N^{++}\right)^2 + \left(\sigma_{N^{++}} RN^{+-}\right)^2\right) \tag{4.3}$$

If we consider, for the moment, only the statistical uncertainty of the pion yield, assuming it to be governed by Poisson statistics, we have that:

$$\left(\frac{\sigma_{A_{LL}}}{A_{LL}}\right)^2 = \left(N^{++} + R^2 N^{+-}\right)\left(\frac{1}{N^2} + \frac{1}{D^2} - \frac{2 \times \text{cov}\left(N, D\right)}{ND}\right) \tag{4.4}$$

where N and D are the numerator and denominator, respectively, of equation 4.2. In the case of small asymmetries such as this, $1/N^2 >> (1/D^2 - (2 \times \text{cov}\left(N, D\right)/ND))$, and the equation reduces to

$$\left(\frac{\sigma_{A_{LL}}}{A_{LL}}\right)^2 = \frac{N^{++} + R^2 N^{+-}}{N^2} \tag{4.5}$$

This is the expression most often used, though it should be noted that in the simplifying limit of $R \approx 1$, we have $\sigma_{A_{LL}} = 1/\sqrt{D}$, as should be expected.

4.1.1 Multiplicity

The straightforward Poisson treatment formulates its statistical variance by treating each pion as an independent event. However, an event with several pions should have

a greater statistical variance than several events with one pion each. To capture this, the statistical variance on a single bin is not its total contents but rather the sum over events of the squares of the multiplicity for that bin.[1] This method treats each bin as an independent Poisson distribution, and considers the correlation of entries within that bin, but not between different bins.

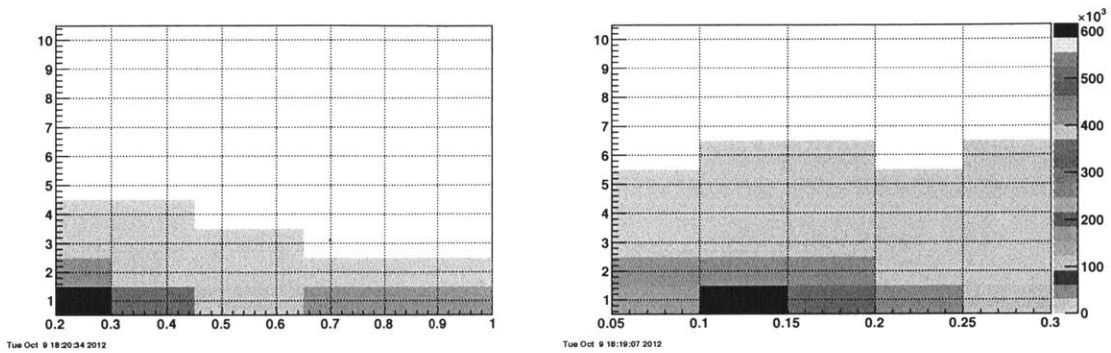

Figure 4-1: Multiplicity of π^+ for each z bin (left) and x bin (right). Pions in a given event should frequently fall into the same x bin, but rarely into the same z bin.

The importance of this correction is obvious in the case of the x binned analysis. All the pions in an event should reconstruct the same x values, but the statistical significance of that event should reflect that it is one event, not the number of pions. The same reasoning follows for z binning, but the effect is much less severe, as a high-z pion is almost by definition alone in an event.

4.2 Jet Energy

Unlike measuring the p_T of a single track, which is good to a few percent[21], measuring the p_T of a jet is much less certain. Because the jet has a fixed cone radius, it cannot be guaranteed to include every fragmented particle, as some particles could fall outside the jet cone. A bigger concern is the amount of energy that will go unde-

[1]This procedure is described in [13, 27, 28] and all point out that by filling the histogram only once per event with weights of the number of pions, ROOT's SumW2() function will take care of the rest. However, because of background subtraction and unfolding involved in this analysis, ROOT is not trusted to handle the errors, and instead the final error bars are multiplied by the RMS multiplicity for each bin.

tected. Some amount of the jet is in the form of long-lived neutral hadrons (neutrons and K_L^0s), which pass through both the tracker and the calorimeter undetected. This fraction varies with every jet, so while it has been corrected for on average, it is impossible to correct for it precisely for a given jet. And lastly, the calorimeter's energy resolution itself plays a role. To calculate the result of all these effects, a Monte Carlo simulation was used to compare the true energy of the jet to its reconstructed energy. This comparison allows for a correction for these effects, and also an estimate of their impact on the overall uncertainty.

4.2.1 Jet Simulation

A sample of events was generated with PYTHIA.[2] For each event, the list of particles from PYTHIA was propagated through a full GEANT[31] based simulation of the detector. The GEANT output was formatted the same way as the STAR detector output, allowing the result to pass through the same analysis chain as the data did.[3] The jet-finding algorithm was run on the simulation after propagation through GEANT, as if it were data, to study jet-finding, measurements, and reconstruction effects.

4.2.2 Jet Unfolding

Due to the uncertainties of jet reconstruction and measurement, a jet with a given true p_T can be reconstructed to a range of p_T values. Conversely, when we measure a jet's p_T, there is a range of true p_T that could have caused it. So given a reconstructed jet with a certain p_T, we would like to know the corresponding range of true p_T. In the language of probability, we are after the conditional probability $p\,(\text{true}|\text{measured})$, which is the probability that a jet has a certain true p_T, given that it was reconstructed with a certain detector p_T.

The PYTHIA simulation generated a distribution of jet p_T, $P(\text{thrown})$. This p_T is referred to as 'true,' and is calculated as the sum of the p_T of all simulated hadrons

[2]PYTHIA[29] is a Monte Carlo program that simulates a hard QCD collision by established PDFs and fragmentation functions determined by the Lund string breaking model.[30]

[3]The 2009 simulation is the largest to date. For details, see [32].

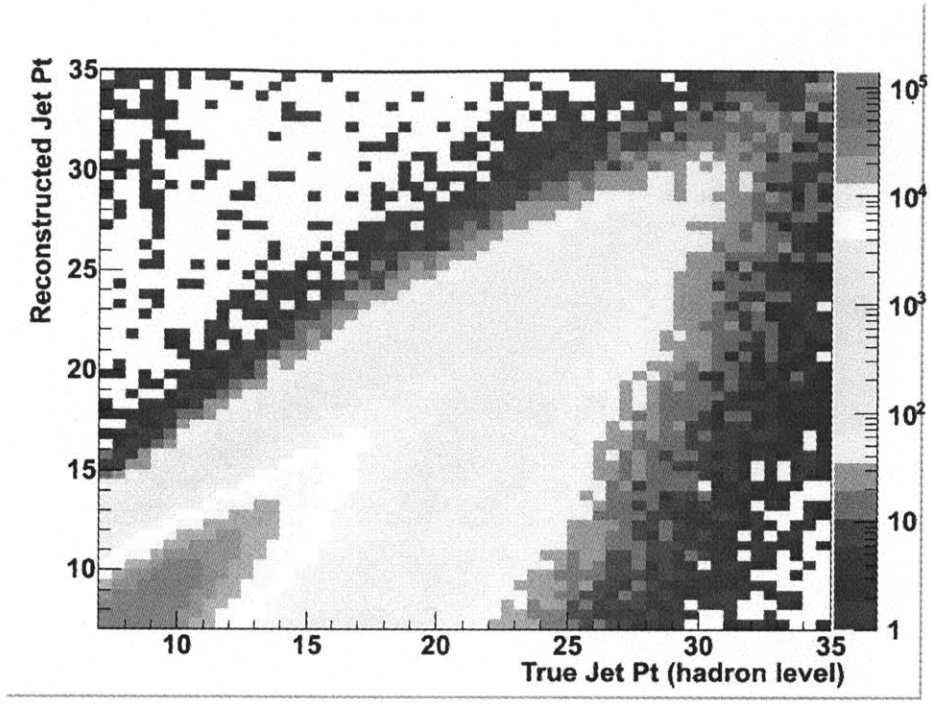

Figure 4-2: The joint distribution of reconstructed jet p_T and true jet p_T.

that fragmented from the same parton. Each simulated event containing a jet was passed through GEANT and STAR's jet-finding algorithm, giving its reconstructed p_T.

The joint distribution of true and reconstructed momenta is used to form the conditional probability $p\,(\text{reco}|\text{thrown})$. The post-GEANT reconstructed distribution $P(\text{reco}) = \sum_{\text{thrown}} P(\text{reco}|\text{thrown})P(\text{thrown})$ quickly follows. It would now be possible to perform a matrix inversion on the smearing matrix, $p\,(\text{reco}|\text{thrown})$. As the smearing matrix is possibly singular, however, there is no guarantee of getting a meaningful answer out of matrix inversion.[4] Instead, we use Bayes' theorem to find that,

$$p\,(\text{thrown}|\text{reco}) = \frac{p\,(\text{reco}|\text{thrown})\,p\,(\text{thrown})}{p\,(\text{reco})}. \tag{4.6}$$

This is not the same as $P(\text{true}|\text{measured})$ because of its dependence on the thrown dis-

[4]Even in the case of non-singular matrices, matrix inversion means the smallest eigenvalues in the forward matrix produce the largest in the inverse. Therefore, the inverse matrix is most heavily dependent on the elements of the forward matrix we know the least about. This is at the heart of all problems with inverting experimental matrices.

tribution. This can be seen in the difference between the reconstructed distribution, $P\,(\text{reco})$, and the actual measured distribution, $P\,(\text{measured})$. If these distributions match exactly, then the thrown distribution is already the true distribution. If not, we can proceed by calculating the "unfolded" distribution

$$\hat{P}\,(\text{thrown}) = P\,(\text{reco}|\text{thrown})\,P\,(\text{measured})$$

and instead of using the result outright, replace $P\,(\text{thrown})$ with $\hat{P}\,(\text{thrown})$ in equation 4.6. The joint and reconstructed distributions are then recalculated, and the whole process can be iteratively repeated until the reconstructed distribution converges to the measured distribution. This iterative method was developed by D'Agostini[33]; it avoids the problems inherent to matrix inversion.

This technique holds not only for jet p_T, but also for any kinematic variable. This means we can unfold directly in our analysis variables, x and z. To unfold in z, the procedure is almost as described previously: we calculate z in events which reconstruct (post-GEANT) to pass all cuts and compare that to the z calculated for the same pion after only PYTHIA. For the analysis binned in x, unfolding proceeds slightly differently. In addition to the detector's effect on jets (as described above), we also want to evaluate the effect of our NLO definitions for x_1 and x_2, found in equation 1.10. So in this case we compare the (post-GEANT) reconstructed x_1 and x_2 directly to the x_1 and x_2 in the PYTHIA record.

With these unfolding matrices, we can easily transform our measured distributions. See Figures 4-3 and 4-4 for the unfolding matrices and their effects. Incorporating this into formula 4.2 and looking at the kth kinematic bin of A_{LL}, we have:

$$A_{LL,k} = \frac{\sum_j \sum_{i\in\text{runs}} P_{Y,i}P_{B,i}(U_{jk}(N_{ij}^{++} + N_{ij}^{--}) - R_i V_{jk}(N_{ij}^{+-} + N_{ij}^{-+}))}{\sum_j \sum_{i\in\text{runs}} P_{Y,i}^2 P_{B,i}^2(U_{jk}(N_{ij}^{++} + N_{ij}^{--}) + R_i V_{jk}(N_{ij}^{+-} + N_{ij}^{-+}))} \tag{4.7}$$

where U_{jk} and V_{jk} are the (almost identical) unfolding matrices for like and unlike sign yields, respectively. They are both derived from the same simulation sample, but are unfolded with their respective binned reconstructed yields. The slight, but

important, nonlinearity of the unfolding process means these two matrices are not exactly the same unless the yields themselves are the same.

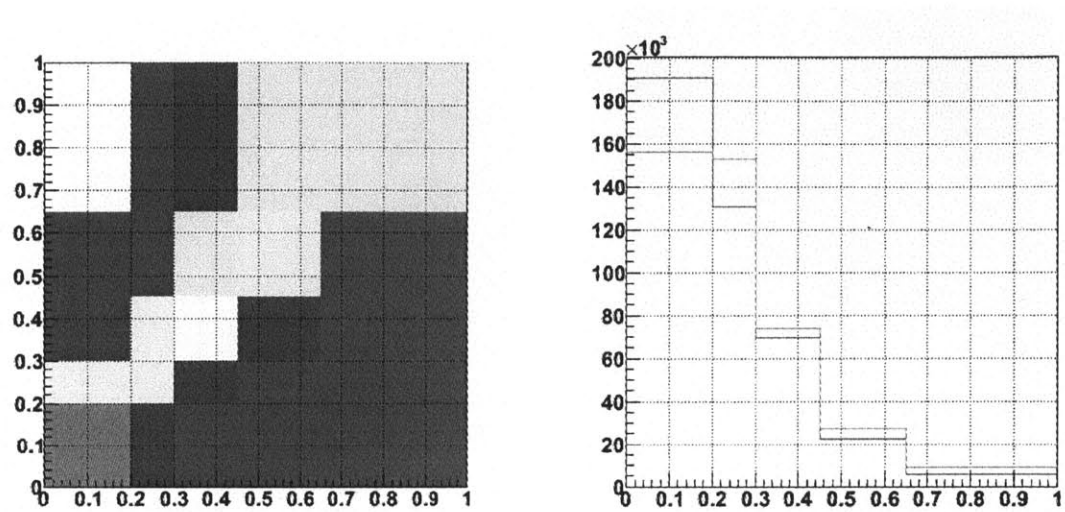

Figure 4-3: An unfolding matrix and its effect: the unfolding matrix for π^+ binned in z (left) and the associated reconstructed (red) and unfolded (blue) distributions (right).

Fundamentally, each row or column in the unfolding matrix represents a multinomial distribution. It follows then that the variance for a multinomial process $\sigma_i^2 = np_i(1-p_i)$ can be used. With the appropriate terms for p_i and n, the variance of the unfolded yield $\hat{n}(C_k) = \sum_j U_{kj} n(E_j)$ is

$$\sigma_k^2 = \sum_j n(E_j) U_{kj} \left(U_{kj} - \sum_i \frac{n(E_i)}{\hat{N}_{true}} U_{ki} \right), \tag{4.8}$$

where $n(E_j)$ is the raw yield in the jth bin, U_{kj} is the unfolding matrix element, and This is calculated for each bin of each spin-dependent yield, and substituted into the expression for $\sigma_{A_{LL}}$, Equation 4.3.

The unfolding process introduces a source of systematic uncertainty in the unfolding matrix itself. Fundamentally, this could be statistical uncertainty (again with multinomial form) based not on the number of measured events, but rather the limited number of simulated events, which as low as 10^5 for some simulated cells. It is

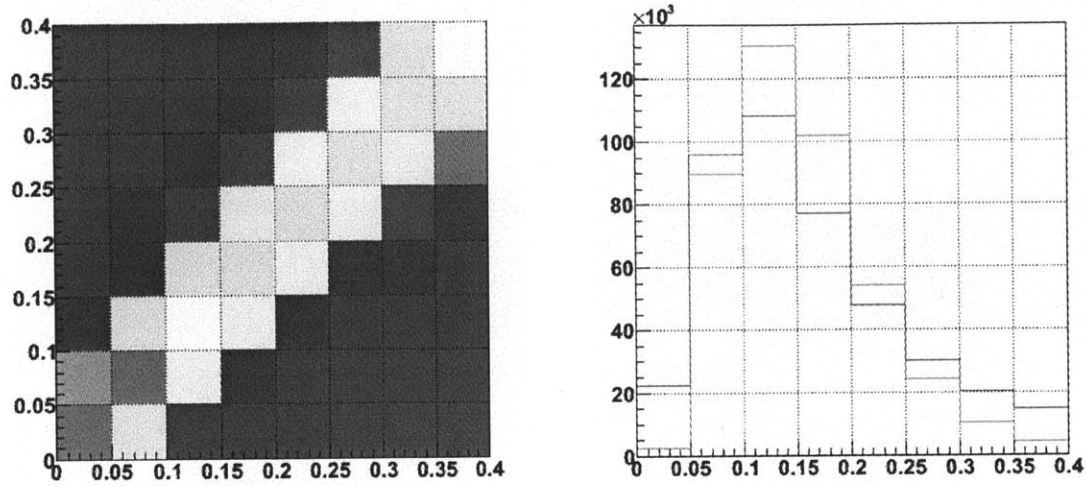

Figure 4-4: The unfolding matrix for π^- binned in x (left) and the associated reconstructed (red) and unfolded (blue) distributions (right). The diagonality of the matrix suggests the NLO approximation (Equation 1.10) is valid.

expressed as:

$$\sigma_k^2 = \sum_{i,j} n(E_i)n(E_j)\mathrm{Cov}\left(U_{ki}, U_{kj}\right), \tag{4.9}$$

where $n(E_j)$ is again the raw yield. The covariance between rows of the unfolding matrix is a function of the matrix itself and the number of events simulated events used to estimate it. The full closed-form expression can be found in [33]. It too is calculated for each yield and analytically propagated through to A_{LL}. However, Equation 4.3, which assumes uncorrelated uncertainties in N^{++} and N^{+-} is incorrect in this case. A change in the matrix would affect spin sorted yields identically, meaning that the associated uncertainties are completely correlated. Instead the effect can be better estimated by treating the sum and difference of these yields (i.e. the numerator and denominator of A_{LL}) as independent. So if N and D are the numerator and denominator, such that $A_{LL} = \frac{1}{P_Y P_B}\frac{N}{D}$, the effect of uncertainties on these quantities on $A_{LL}$is:

$$\sigma_{A_{LL}} = \frac{1}{P_Y P_B}\sqrt{\frac{\sigma_N^2}{D^2} + \frac{\sigma_D^2 N^2}{D^4}} \tag{4.10}$$

The result of this calculation can be found in Table 4.4.

4.3 Background Subtraction

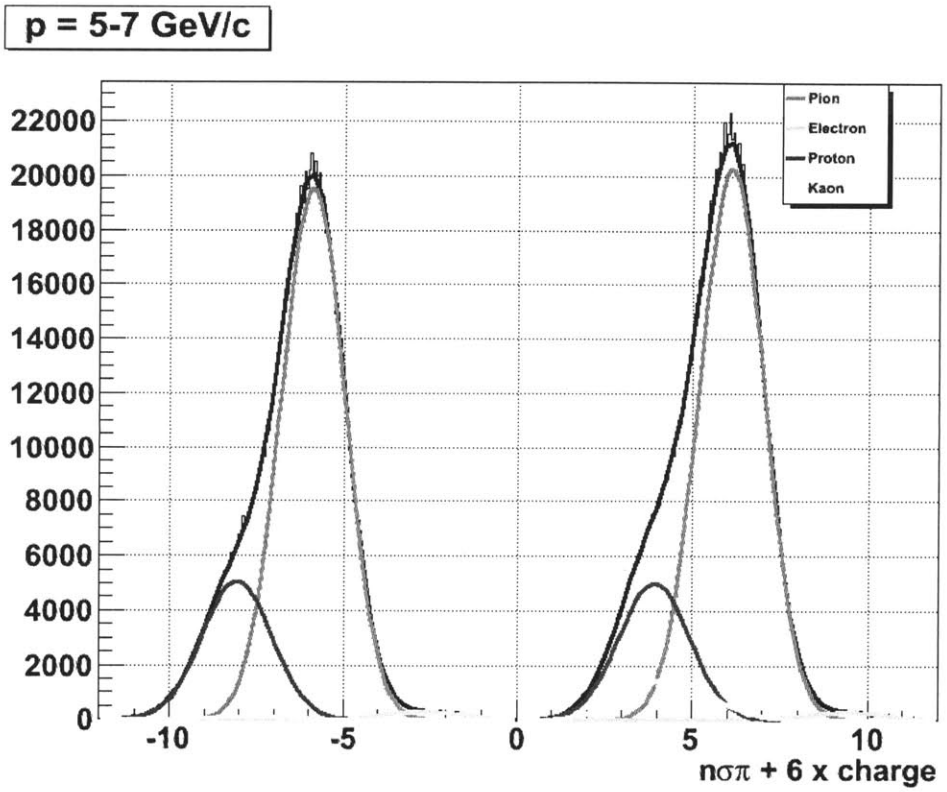

Figure 4-5: A simultaneous fit of distributions in $n\sigma_\pi$ for all particle species and both charges.

Figure 4-5 shows an $n\sigma_\pi$ distribution for the 5-7 GeV/c momentum bin, separated by 10×charge, so as to fit positive and negative particles simultaneously. The fit function shown is a sum of eight Gaussian distributions, one for each type of particle. The fit is performed with the constraints that all species have the same Gaussian width, and that both charges have the same mean for each particle type.[5]

We established a selection window for the signal such that any track residing between certain values of $n\sigma_\pi$ could be regarded as a pion. We also established $n\sigma_\pi$ values that defined the sideband windows for electrons or for protons and kaons. See Table 4.1 for these parameters.

[5]The yields of different particles, however, are functions of charge. Electrons and positrons are produced in pairs, and thus have the same yields. But protons have much more up quark content than strange quark, so there is a large imbalance in favor of K^+ over K^-.

Track p_T	Pion Window	Proton/Kaon Max	Electron Min
2.0-3.2	(-1.1,2.3)	-2.1	2.6
3.2-4.6	(-1.4,2.1)	-2.1	2.4
4.6-6.3	(-1.4,1.8)	-2.1	2.4
6.3-8.8	(-1.4,1.8)	-2.1	2.4
8.8-13	(-1.3,1.4)	-2.1	2.1

Table 4.1: Values of $n\sigma_\pi$ used for particle identification.

Once both signal and sideband windows were established, all events were sorted into those three windows.

Pions, the lightest of light quark mesons, are produced much more than baryons (protons), strange mesons (kaons), or electroweak particles (electrons). A track picked at random will most likely be a pion. In addition, the spectra in $n\sigma_\pi$ separate pions from other species by more than one standard deviation. Nevertheless, there is an overlap: even a very small selection window in $n\sigma_\pi$ would have a tiny contamination from other particles.

The asymmetry as measured, A_{LL}^{RAW}, contains primarily the true asymmetry, $A_{LL}^{\pi,true}$, but is contaminated by fractional contributions of the A_{LL}s from the other particles.

$$A_{LL}^{\pi,RAW} = (1 - f(p+k) - f(e))\, A_{LL}^{\pi,true} + f(p+k) A_{LL}^{(p+k),true} + f(e) A_{LL}^{e,true} \tag{4.11}$$

where f is the background fraction:

$$f_x(y) = \frac{x \text{ counts in } y \text{ window}}{\text{total count in } y \text{ window}}$$

If the sideband A_{LL}s were estimated from theory or otherwise known a priori, these simple background fractions would suffice. Because these sidebands are measured as well, they contain contamination from the signal itself. Instead, reduced background fractions, f', are used.

$$f'(x) = \frac{f_x(\pi)}{1 - f_\pi(x)}$$

The background fraction is termed 'reduced,' as it accounts for both the contamina-

tion of the signal and the contamination of the background by the signal.

These reduced background fractions are used to remove sideband contamination from the raw pion A_{LL},

$$A_{LL}^{\pi} = \frac{A_{LL}^{RAW} - f'(p+k)A_{LL}^{(p+k)} - f'(e)A_{LL}^{e}}{1 - f'(p+k) - f'(e)} \tag{4.12}$$

where the asymmetries for the sideband signals, $A_{LL}^{(p+k)}$ and A_{LL}^{e}, are measured in the same way as for the central pion signal, A_{LL}^{RAW}. (See Equation 4.2.)

Because the A_{LL}s for the sidebands are also a measured quantities, the statistical uncertainty on the pion A_{LL} is now increased.

$$\sigma_{A_{LL}^{\pi}} = \frac{\sqrt{\sigma^2_{A_{LL}^{RAW}} + f'(p+k)^2\sigma^2_{A_{LL}^{(p+k)}} + f(e)^2\sigma^2_{A_{LL}^{e}}}}{1 - f'(p+k) - f'(e)} \tag{4.13}$$

Because both the background fractions and the sideband A_{LL}s are small, the correction to the pion A_{LL} they cause is almost negligible. However, the increases to the statistical uncertainties are substantial.

4.4 Relative Luminosity

To measure luminosity, two sets of dedicated high speed detectors were used: the BBC and ZDC, described in section 2.2.3. Both were configured in pairs to record coincident events, which are more robustly indicative of central events. Unlike most other detector subsystems, the read out of luminosity detectors was not triggered. Instead, a simple threshold measurement was recorded at high rate. To make this possible, a dedicated collection of Field Programmable Gate Arrays, known as the scaler boards, was used to record important luminosity information for each bunch crossing. The scalers incremented the value at a memory address corresponding to a certain condition every time that condition was met. For example, there was a memory address that corresponded to the East ZDC and both BBC's over threshold on bunch crossing number 53. The value at that address represented how many times

such a configuration had occurred.

4.4.1 Accidental and Multiple Coincidence Corrections

There are two biases implicit in this type of recording scheme. They both result from situations where the coincidence rate is not linearly related to the instantaneous luminosity. The first is when two single side events happen in that time frame and register as a coincidence. The rate of single events will increase with instantaneous luminosity. Consequently, this sort of accidental coincidence will increase with the square of luminosity, and should be compensated for. The second bias is caused by the system's inability to record more than one coincidence at a time, leading to a non-linear underestimation.

To compensate for these mechanisms we use four quantities: N_{EW}, the raw number of recorded coincidences; N_E and N_W, the East and West (respectively) singles counts; and N_{BC}, the number of times a bunch crossing has been recorded.

To compensate for the accidental coincidences, we subtract the product of single hit probabilities ($P_E = N_E/N_{BC}$) from the probability of any coincidence ($P_{EW} = N_{EW}/N_{BC}$). Properly normalized, P_C, the probability of a 'true' coincidence, is

$$P_C = \frac{P_{EW} - P_E P_W}{1 + P_{EW} - P_E - P_W}.$$

For the multiple event correction, we estimate the effect by assuming a Poisson distribution of coincidences and using the number of non-events (crossings with no hits observed) to determine the rate.

$$P_0 = e^{-\mu} = 1 - P_C,$$

Together, N_C, the corrected coincidence yield, becomes:

$$N_C = -N_{BC} \cdot \ln\left(1 - \frac{N_{EW} - \frac{N_E N_W}{N_{BC}}}{N_{BC} + N_{EW} - N_E - N_W}\right) \tag{4.14}$$

This was done for both detectors, and for each bunch crossing, before any sorting by spin pattern. These corrections were developed at Fermilab. A full derivation can be found in [34].

4.4.2 Relative Luminosity Uncertainties

The statistical uncertainty on the BBC-derived relative luminosity is small enough to be negligible. Other analyses[13] have computed A_{LL} with both the BBC and ZDC values and used the resulting difference as a systematic uncertainty. In the case of this analysis, the result from such a comparison was a negligible 10^{-6}. Instead, this analysis used the most conservative estimate of 0.00015 from a dedicated relative luminosity analysis.[35] This is still smaller than the unfolding matrix uncertainty in the higher kinematic bins.

4.4.3 False Asymmetries

To test the validity of polarization and relative luminosity information, we construct several other asymmetries, which by parity arguments should be identically zero. To do this we must first construct several luminosity ratios:

$$R_1 = \frac{L^{++} + L^{-+}}{L^{+-} + L^{--}} \qquad R_4 = \frac{L^{++}}{L^{--}}$$

$$R_2 = \frac{L^{++} + L^{+-}}{L^{-+} + L^{--}} \qquad R_5 = \frac{L^{-+}}{L^{--}}$$

$$R_3 = \frac{L^{++} + L^{--}}{L^{+-} + L^{-+}} \qquad R_6 = \frac{L^{+-}}{L^{--}}$$

R_3 is the relative luminosity used for A_{LL}, referred to previously as just R. All others are used for these systematic checks.

The first of these checks is for single-spin asymmetries, which are asymmetries defined by the helicity of only one beam. Figure 4-6 shows that, for both beams and pion charges, these asymmetries were found to be consistent with zero.

$$A_L^B = \frac{1}{P_B} \frac{N^{++} + N^{+-} - R_1 \left(N^{-+} + N^{--}\right)}{N^{++} + N^{+-} + R_1 \left(N^{-+} + N^{--}\right)}$$
$$A_L^Y = \frac{1}{P_Y} \frac{N^{++} + N^{-+} - R_2 \left(N^{+-} - N^{--}\right)}{N^{++} + N^{+-} + R_2 \left(N^{-+} + N^{--}\right)}$$

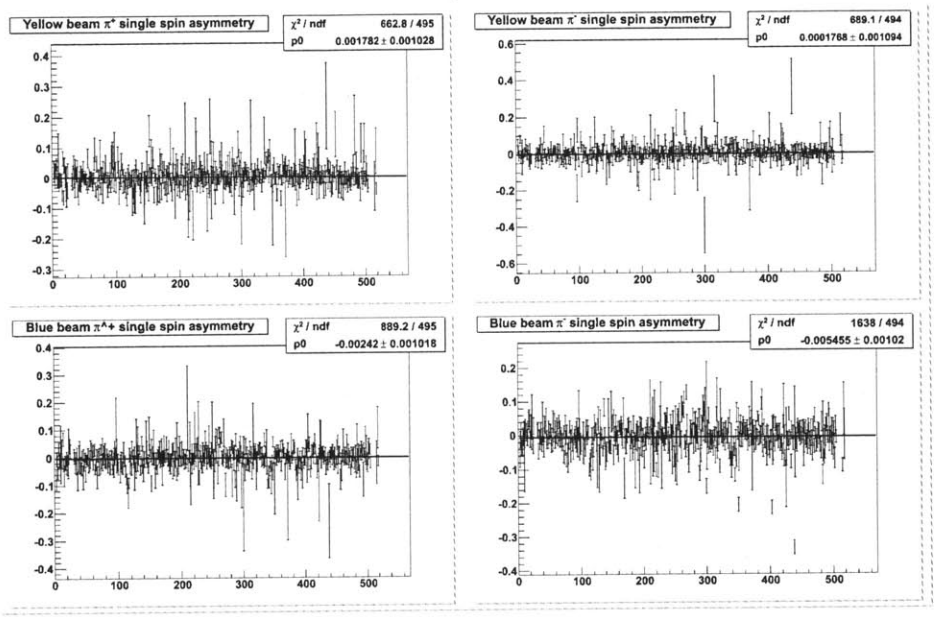

Figure 4-6: The single-spin false asymmetries as a function of run number.

The other check is for the 'like-sign' and 'unlike-sign' false asymmetries. These are created by contrasting the yields of spin configurations with the same total spin. Again, by parity arguments, these yields should be the same. Figure 4-7 shows these asymmetries are also consistent with zero.

$$A_{LL}^{\text{Like}} = \frac{1}{P_Y P_B} \frac{N^{++} - R_4 N^{--}}{N^{++} + R_4 N^{--}}$$
$$A_{LL}^{\text{Unlike}} = \frac{1}{P_Y P_B} \frac{R_6 N^{+-} - R_5 N^{-+}}{R_6 N^{+-} + R_5 N^{-+}}$$

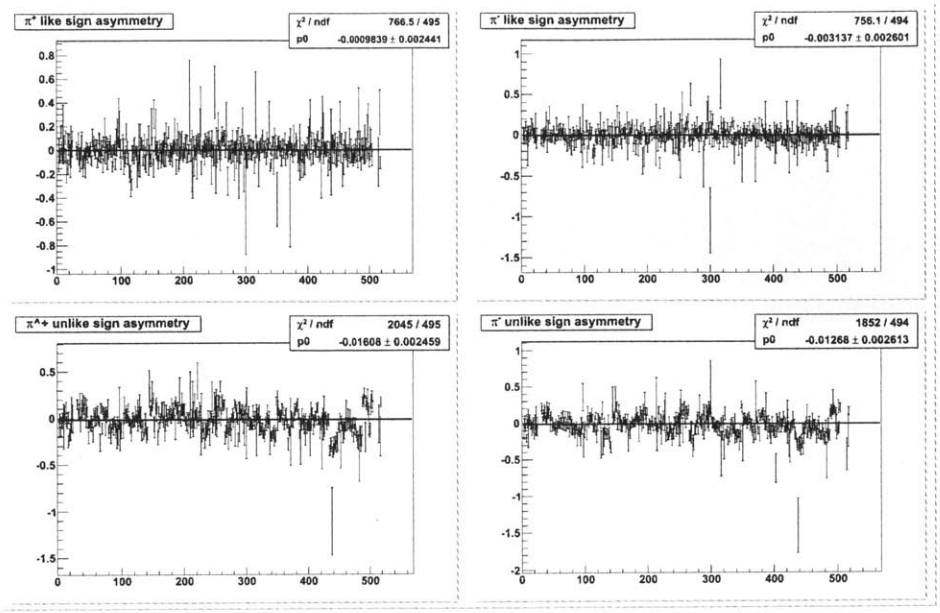

Figure 4-7: The like- and unlike- sign false asymmetries as a function of run number.

By seeing that all the false asymmetries are consistent with zero, we can be sure there are no strange issues with polarization, relative luminosity measurements, or spin sorting.

4.5 Polarization

Polarization measurements from the CNI polarimeters (Section 2.1.3) were taken at the beginning of every fill several times thereafter. These measurements were averaged together in a luminosity dependent fashion such that one value of polarization for each beam can be used for every run in a fill.[36] Figure 4-8 shows the polarization performance on this by-fill basis, and Table 4.2 shows the average polarization across the entire 2009 dataset.

	Average Polarization	Uncertainty ($\Delta P/P$)
Blue Beam	59%	4.7%
Yellow Beam	59%	4.7%

Table 4.2: Average polarization performance.

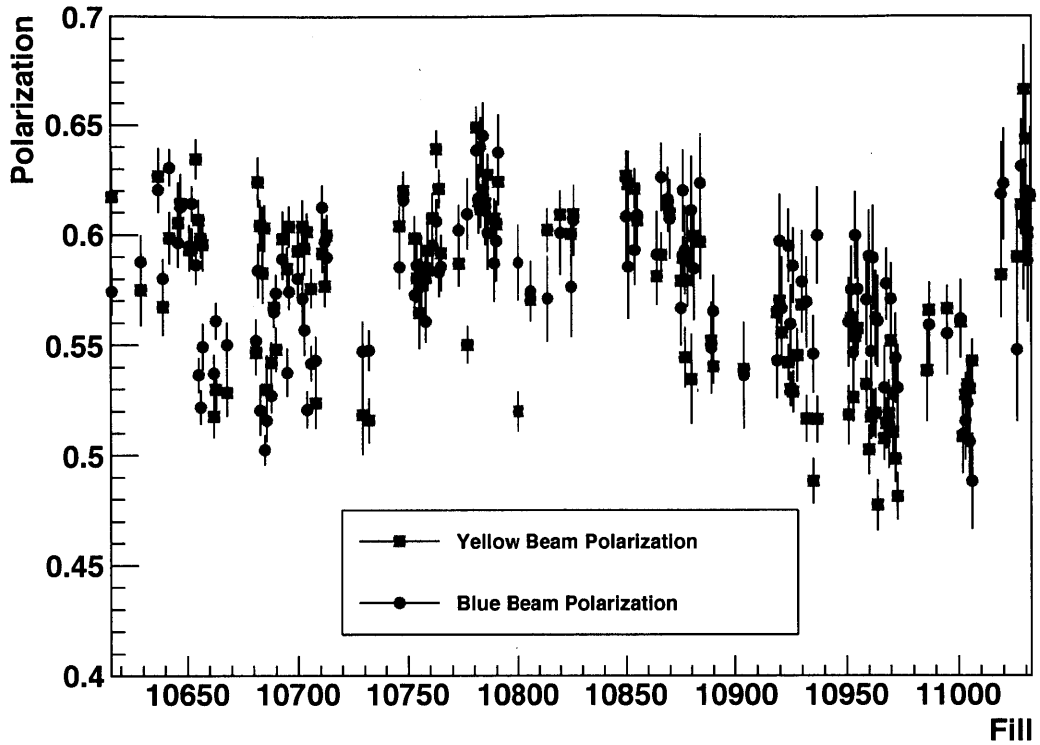

Figure 4-8: Polarization by fill.[32]

4.5.1 Beam Transverse Component

If the spins of the incoming protons were not rotated to perfectly longitudinal, the asymmetry measured will actually be a combination of A_{LL} and A_{NN}, a transverse asymmetry. The 2009 inclusive jet study[37] has shown that the most this transverse beam component could be is 0.025%. This adds a systematic error of $\delta A_{LL} = 0.00025$.

4.6 Summary of Statistical Uncertainties

As mentioned in sections 4.1.1 and 4.2.2, due to unfolding and multiplicity considerations, the statistical uncertainty on A_{LL} is slightly more involved than just Poissonian square root errors. Table 4.3 shows the raw yields, the Poisson errors, the unfolded multinomial errors, and the effect of the multiplicative multiplicity factor.

	z	N	$1/\sqrt{D}$	**Unfolded**	**Multiplicity**	**Background**
π^-	**0.2 - 0.3**	241181	0.00593	0.00261	0.00282	0.00608
	0.3 - 0.45	120871	0.00838	0.00503	0.00523	0.00927
	0.45 - 0.65	36635	0.01522	0.00961	0.00972	0.01488
	0.65 - 1.0	8572	0.03147	0.01981	0.01984	0.02629
π^+	**0.2 - 0.3**	259104	0.00572	0.00254	0.00276	0.00631
	0.3 - 0.45	138205	0.00784	0.00470	0.00492	0.00954
	0.45 - 0.65	45034	0.01373	0.00869	0.00881	0.01542
	0.65 - 1.0	11704	0.02693	0.01727	0.01731	0.02692

Table 4.3: Statistics summary

4.7 Summary of Systematic Uncertainties

All systematic uncertainties associated with reconstruction and yields are encompassed into the unfolding uncertainty. The other uncertainties which influence the asymmetry directly are the beam transverse component and the relative luminosity uncertainty. Table 4.4 shows the systematic uncertainties due to these sources, as well as their sum in quadrature.

	z	A_{LL}	**Rel. Lumi.**	**Transverse**	**Total**
π^-	**0.2 - 0.3**	0.00001	0.00015	0.00025	0.00029
	0.3 - 0.45	0.00029	0.00015	0.00025	0.00041
	0.45 - 0.65	0.00044	0.00015	0.00025	0.00053
	0.65 - 1.0	0.00599	0.00015	0.00025	0.00600
π^+	**0.2 - 0.3**	0.00002	0.00015	0.00025	0.00029
	0.3 - 0.45	0.00019	0.00015	0.00025	0.00035
	0.45 - 0.65	0.00066	0.00015	0.00025	0.00072
	0.65 - 1.0	0.00858	0.00015	0.00025	0.00859

Table 4.4: Systematics summary

THIS PAGE INTENTIONALLY LEFT BLANK

Chapter 5

Results and Conclusions

This thesis measured the charged pion and jet A_{LL} for the 2009 200-GeV run. The numerical results are provided in Table 5.1. This measurement adds to the world

	z	$A_{LL}(\times 10^{-3})$	$\sigma_{A_{LL}}(\times 10^{-3})$	x	$A_{LL}(\times 10^{-3})$	$\sigma_{A_{LL}}(\times 10^{-3})$
	0.2-0.3	-5.16	± 5.88	0.05-0.10	4.12	± 6.88
	0.3-0.45	14.06	± 8.90	0.10-0.15	4.86	± 6.44
π^-	0.45-0.65	7.85	± 14.31	0.15-0.20	1.25	± 6.70
	0.65-1.0	18.15	± 25.39	0.20-0.25	7.36	± 7.38
				0.25-0.30	11.69	± 9.13
	0.2-0.3	6.86	± 6.11	0.05-0.10	13.59	± 7.27
	0.3-0.45	12.76	± 9.16	0.10-0.15	10.91	± 6.77
π^+	0.45-0.65	17.55	± 14.88	0.15-0.20	6.41	± 7.06
	0.65-1.0	39.92	± 26.73	0.20-0.25	1.84	± 7.95
				0.25-0.30	5.82	± 9.64

Table 5.1: Final results for both charges and both binnings.

knowledge of the proton's gluon polarization and can be interpreted through comparison to theoretical predictions. Figures 5-1, 5-2, and 5-3 all show the measured A_{LL}s plotted alongside predictions made by two leading models: DSSV and GRSV.

5.1 Theory and Comparison

Theoretical predictions for this channel were made by NLO calculations using DSSV, GRSV-std. Binned in z, as shown in Figures 5-1 and 5-2, the data indicates ΔG is

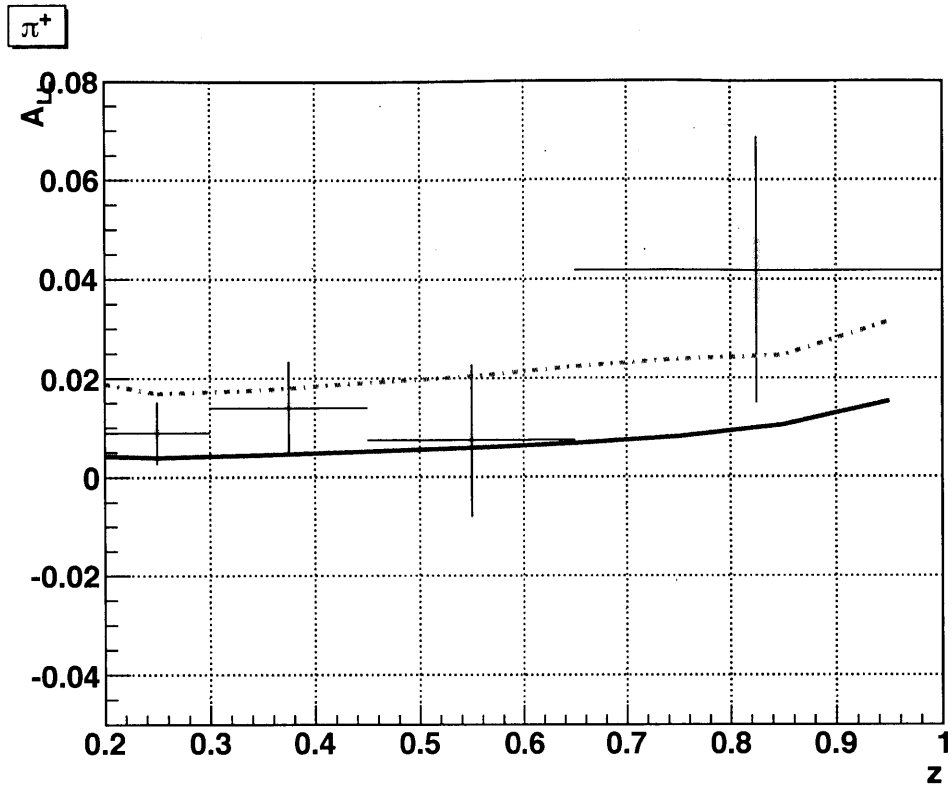

Figure 5-1: The π^++jet A_{LL} as a function of z.

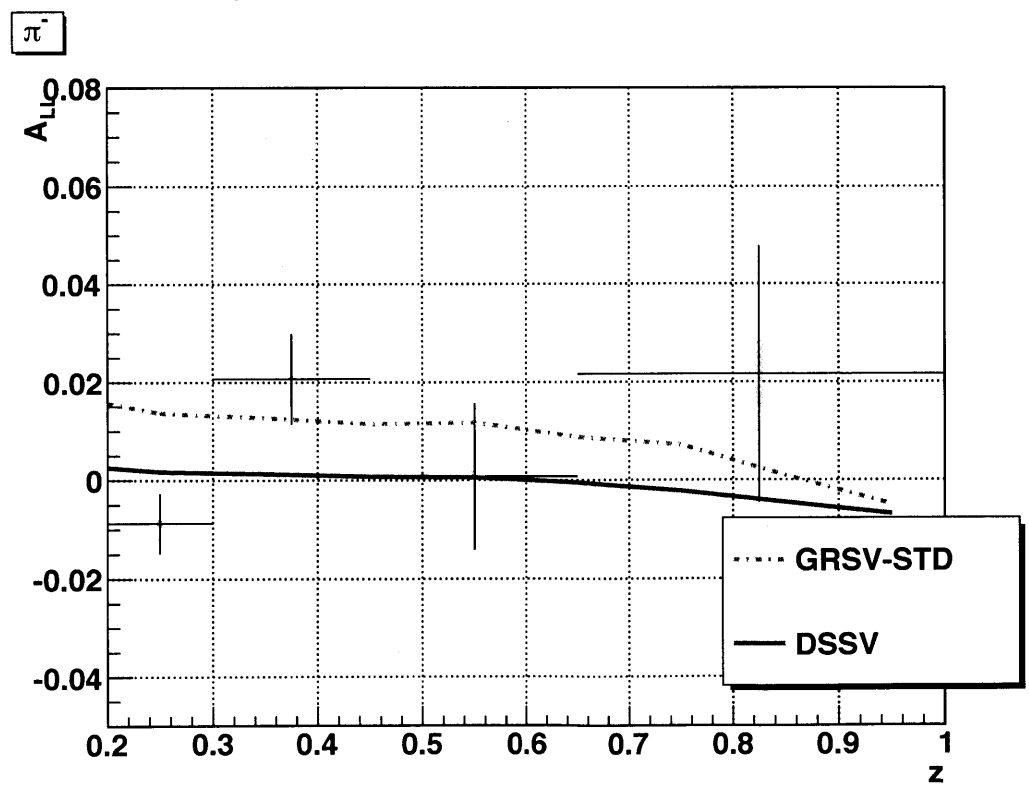

Figure 5-2: The π^-+jet A_{LL} as a function of z. The vertical black bars show the statistical uncertainties, while the green bars show the systematic uncertainties.

slightly larger than predicted by DSSV, but not as large as predicted by GRSV-std. This result suggests that ΔG is of a similar size to $\Delta\Sigma$, which is consistent with other recent measurements of A_{LL} for inclusive jets, di-jets, and neutral pions. The inclusive jet result[37], which has the highest statistics, is included for completeness as Figure 5-4.

Binned in x, as shown, in Figure 5-3, the data suggest a similar trend, and while they are consistent with both theory curves, they could better be described by a trend that represents an average in between DSSV and GRSV-std. It is worth noting though, that even though x_1 and x_2 are kinematically anti-correlated, the results using x_1 and x_2 are identical, as they should be.

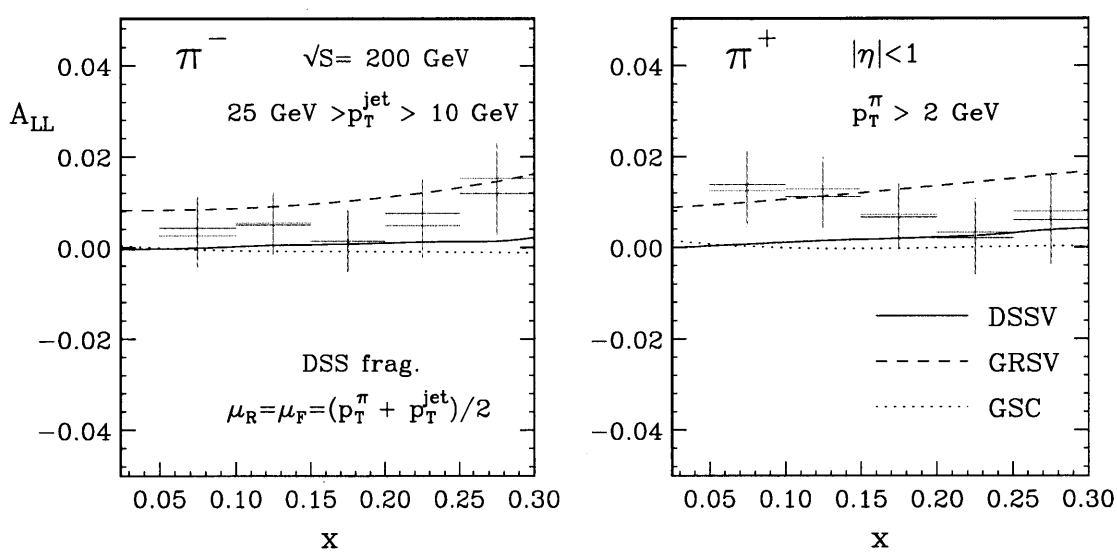

Figure 5-3: The π^-+jet and π^++jet A_{LL}s as a function of x. Note the agreement of the analysis using x_1, in red, to that using x_2, in blue.

5.2 Agreement with Previous Results

An analysis of the same channel was also done for the 2006 run at STAR.[27] This new measurement mostly improves on the old by gathering more statistics and handling systematic effects differently, but the measurements are consistent. The binning for this analysis was chosen to facilitate quick comparison and combination. Figure 5-5

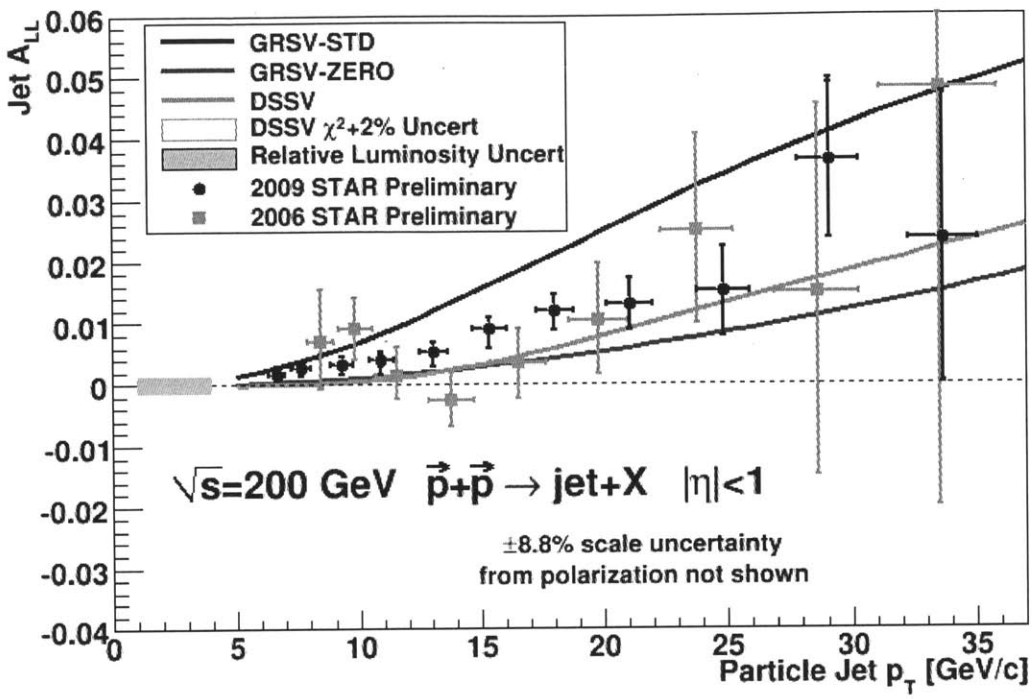

Figure 5-4: The 2009 inclusive jet A_{LL}result[37] similarly suggests a ΔG larger than that predicted by DSSV, yet not as large as that used by GRSV-std.

shows a direct comparison between the 2009 and 2006 measurements, while Figure 5-6 shows the combined result. The two measurements were combined using an uncertainty weighted average, which is computed for each bin as:

$$A_{LL,\text{combined}} = \frac{\sigma_{2009} A_{LL,2006} + \sigma_{2006} A_{LL,2009}}{\sigma_{2006} + \sigma_{2009}} \tag{5.1}$$

The combined uncertainty[1] follows as:

$$\sigma_{\text{combined}} = \sqrt{2} \frac{\sigma_{2006}\sigma_{2009}}{\sigma_{2006} + \sigma_{2009}}$$

Figure 5-6 shows the 2006 result in gray, the 2009 result in green, and the combined result in blue. This result agrees best with DSSV, which can be seen in Table 5.2. Confidence levels[2] are computed as the integral of the χ^2 distribution greater than

[1]In combining results, the asymmetric error bars in the 2006 analysis were replaced by symmetric ones, giving a very slight change to the confidence levels.

[2]When comparing a measurement to a null hypothesis, confidence levels are called p-values.

the measured χ^2:

$$\mathrm{CL} = 1 - \frac{\gamma(\frac{\chi^2}{2}, \frac{\mathrm{NDF}}{2})}{\Gamma(\frac{\mathrm{NDF}}{2})} \tag{5.2}$$

where NDF is the number of degrees of freedom (4 in this case), and Γ and γ are, respectively, complete and incomplete gamma functions.

However, these χ^2 values and associated confidence levels are most dependent on the bins with the smallest (experimental) uncertainties. These are the bins lowest in z, which have the greatest statistical yield. Paradoxically, these are the same bins where the theory is most uncertain because of relatively less understood fragmentation functions and associated polarized PDFs.[3] If the lowest z bin is excluded from the confidence level calculations, neither theory can be ruled out, and in fact GRSV-std is marginally more compatible with the 2009 result than DSSV. For the three bins only, the combined π^+ result agrees with DSSV at 0.35, and with GRSV-std at 0.25, while the combined π^- result has DSSV at 0.66 and GRSV-std at 0.85. So χ^2 analyses cannot be taken as definitive if they depend so heavily on the physically uninteresting regime. Nevertheless, they provide a quantitative measure of agreement and an indication of statistical sensitivity.

The x bins share statistical sensitivity more evenly than the z bins. The χ^2 analysis of the x binned result thus gives conservative confidence levels consistent with the three-bin confidence levels for z. The x binned π^+ result agrees with DSSV at 0.37, and with GRSV-std at 0.34, and the x binned π^- result agrees with both theories at 0.73.

The results still lack the statistical precision to conclusively eliminate either of the two theories. If the same values were measured with smaller uncertainties, the result would still not suggest one theory over the other. Far from being uninformative, this suggests again that the true value of Δg lies between these two theoretical predictions.[4]

[3]Theoretical uncertainties are not included in the χ^2 analysis.

[4]The arithmetic mean of the two theory curves agrees with the x binned π^- result with a χ^2/NDF of 0.56/5 and thus a confidence level of 99%.

Gluon polarization scenario	Confidence Level					
	2006		2009		Combined	
	π^-	π^+	π^-	π^+	π^-	π^+
GRSV-STD	0.58	0.18	0.13	0.0006	0.07	0.0005
DSSV	0.98	0.59	0.62	0.17	0.76	0.34

Table 5.2: Confidence levels for the two leading theoretical models with respect to the z-binned results.

5.3 Future Measurements

Upcoming RHIC runs promise higher luminosities and polarizations, which will allow future measurements to better constrain Δg. In principle, a larger simulation sample would help to reduce systematic uncertainty, but as the 2009 simulation was already sizable[5] it is not likely to be improved upon. In any case, the measurement is limited by statistics and not systematics, so more data will continue to offer the greatest promise for an improved measurement. The next data set of polarized proton collisions at STAR will provide further exciting and sensitive results.

[5]Approximately 10 cpu years.[32]

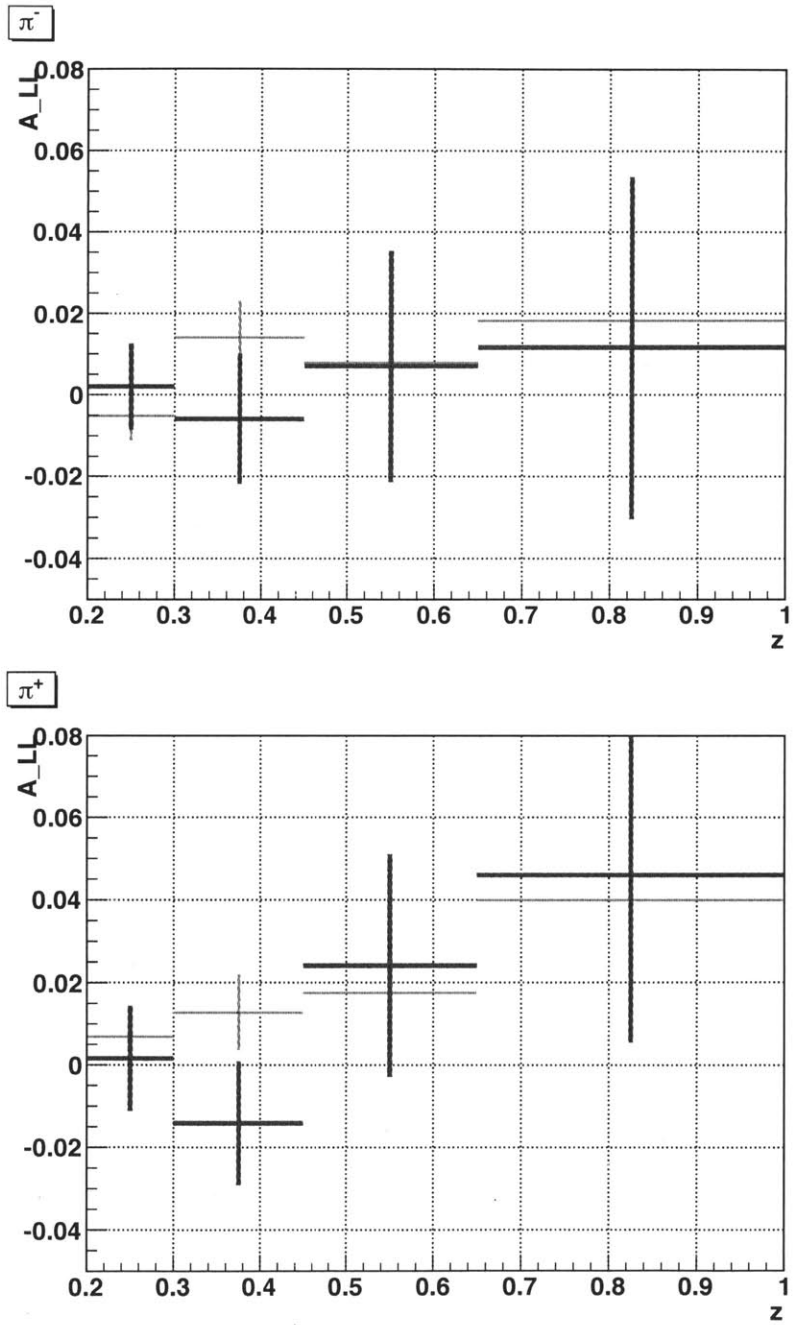

Figure 5-5: The 2006 (blue) and 2009 (red) A_{LL}s as a function of z. The results agree well, especially at high z.

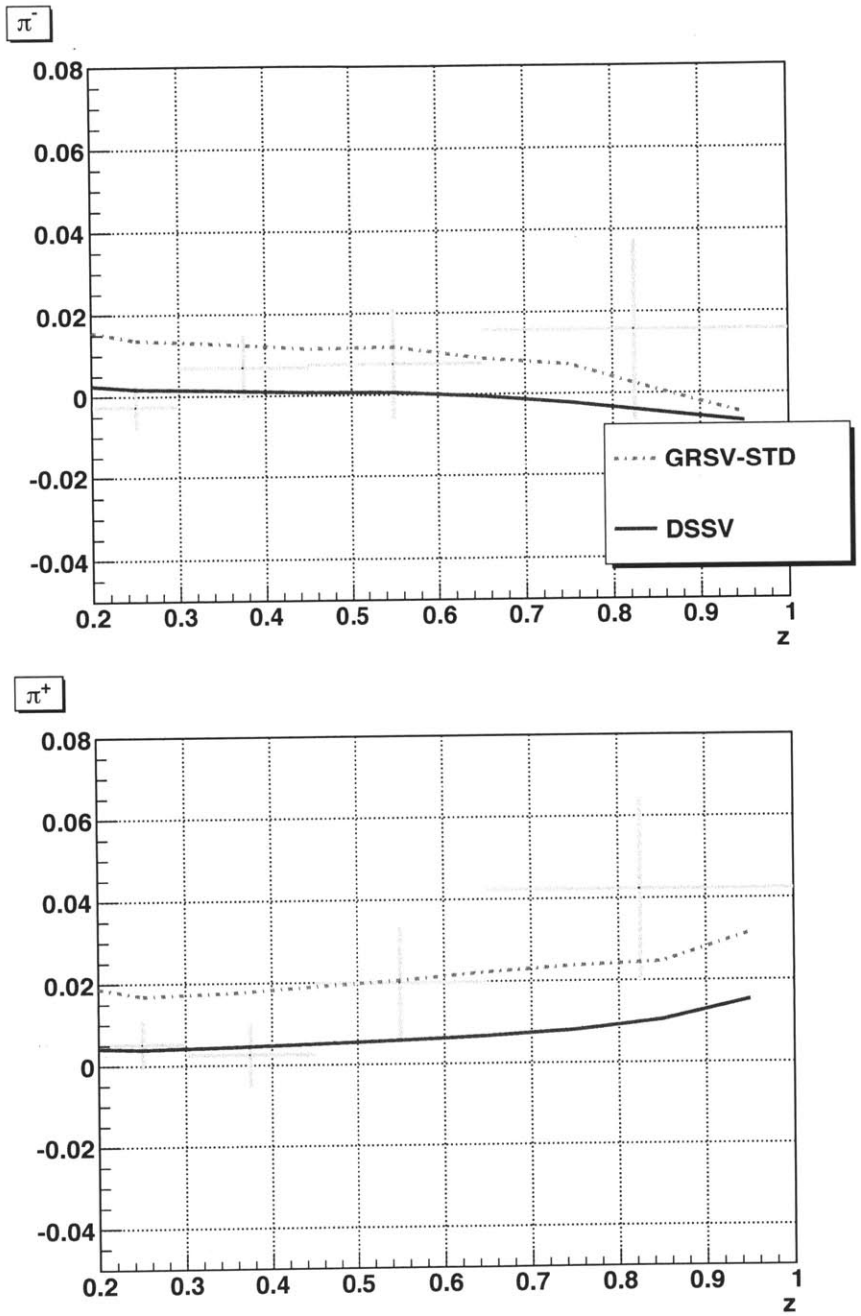

Figure 5-6: The combined A_{LL}s as a function of z. The combination smooths out the results at low z, but leave intact the high z conclusion that $A_{LL}$is higher than theory.

Appendix A

Comparison of Data to Simulation

An unfolding based on simulation must be motivated by a simulation which accurately depicts the measured physics. Figure A-1 shows that the yield of positive pions binned in x is indeed well modeled by the simulation. The curves are integral normalized for comparison and the functional forms of the two spectra agree.

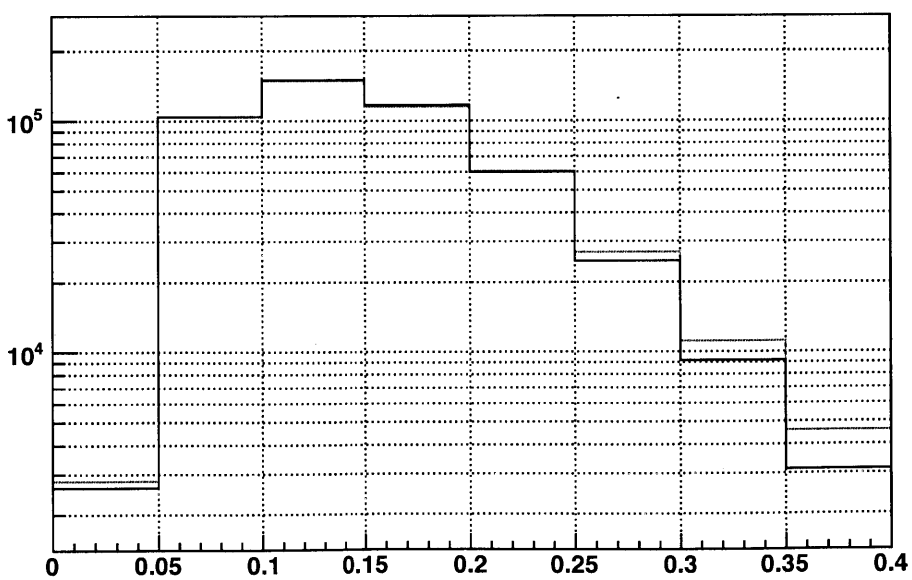

Figure A-1: Spectra in x for positive pions in both data (red) and simulation including Geant (black). The lowest and two highest bins are not included in the A_{LL} analysis.

The agreement is preserved after unfolding as well, as shown in Figure A-2.

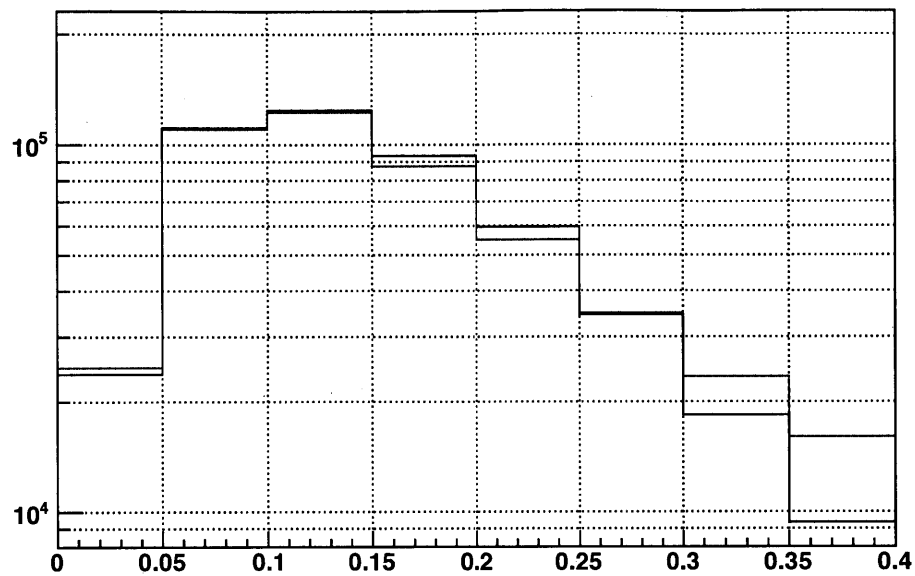

Figure A-2: Spectra in x for positive pions in unfolded data (blue) and raw Pythia simulation (black). Again, the lowest and two highest bins are not included in the A_{LL} analysis.

Viewed in a certain light, this is completely unsurprising. While beginning the unfolding routine with an accurate thrown distribution makes convergence easier and faster, the motivation for the scheme is to remove dependence on the thrown simulation. In fact, D'Agostini notes that even a flat distribution should suffice. To illustrate this point, Figure A-3 shows precisely that: the blue line is the same unfolded distribution as in Figure A-2, but the red is the distribution unfolded using the the distribution with the Pythia sample re-weighted to be flat before iteration.

The situation is the same for negative pions and for the z binning. In all cases, the simulation agrees well with data. However, because of the iterative techniques used, this is not a stringent requirement.

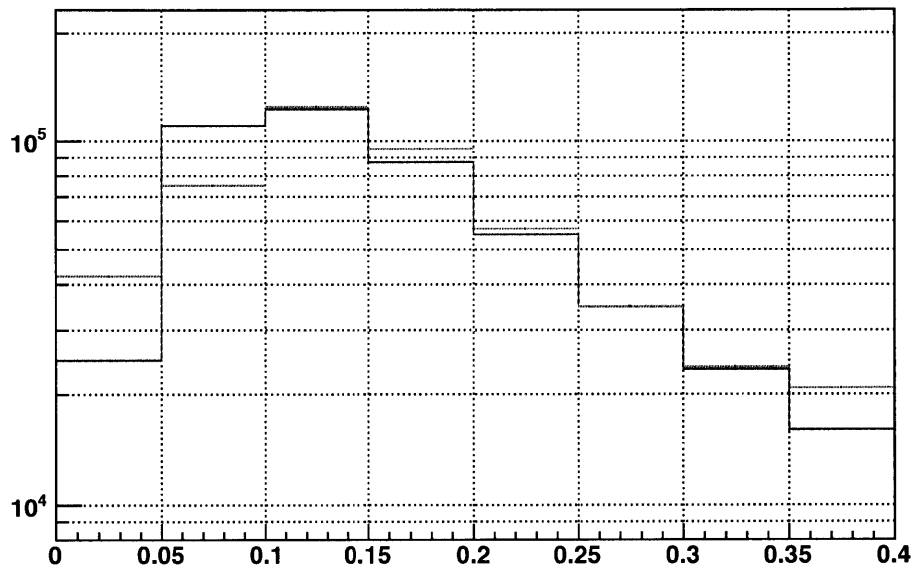

Figure A-3: Spectra in x for positive pions in data unfolded by the usual fashion (blue) and by a simulation sample initialized to flat (red) after only a dozen iterations.

THIS PAGE INTENTIONALLY LEFT BLANK

Appendix B

Additional Tables and Graphs

B.1 Unfolding Matrices

The values of the unfolding matrices used are reproduced here. Tables B.1 and B.4 correspond to Figures 4-3 and 4-4, respectively.

z	0.0 - 0.2	0.2 - 0.3	0.3 - 0.45	0.45 - 0.65	0.65 - 1.0
0.0 - 0.2	0.90649	0.30906	0.01757	0.00056	0.00000
0.2 - 0.3	0.09221	0.62704	0.28247	0.02240	0.00185
0.3 - 0.45	0.00128	0.06337	0.64966	0.36391	0.05326
0.45 - 0.65	0.00002	0.00052	0.04969	0.56933	0.42044
0.65 - 1.0	0.00000	0.00001	0.00061	0.04380	0.52445

Table B.1: The unfolding matrix for π^+ binned in z.

z	0.0 - 0.2	0.2 - 0.3	0.3 - 0.45	0.45 - 0.65	0.65 - 1.0
0.0 - 0.2	0.90764	0.31217	0.01935	0.00089	0.00000
0.2 - 0.3	0.09114	0.62524	0.28930	0.02632	0.00225
0.3 - 0.45	0.00123	0.06208	0.64205	0.37010	0.05752
0.45 - 0.65	0.00000	0.00051	0.04870	0.56126	0.42959
0.65 - 1.0	0.00000	0.00000	0.00060	0.04144	0.51064

Table B.2: The unfolding matrix for π^- binned in z.

x	0.0-0.05	0.05-0.1	0.1-0.15	0.15-0.2	0.2-0.25	0.25-0.3	0.3-0.35	0.35-0.4
0.0-0.05	0.55957	0.14512	0.03587	0.01599	0.00645	0.00313	0.00286	0.00584
0.05-0.1	0.37782	0.58550	0.24394	0.08278	0.03844	0.01706	0.01147	0.01957
0.1-0.15	0.03166	0.20346	0.43795	0.23366	0.09359	0.04536	0.02835	0.02601
0.15-0.2	0.01246	0.03479	0.19345	0.34577	0.20707	0.08941	0.05062	0.04028
0.2-0.25	0.00747	0.01247	0.05330	0.19670	0.30491	0.19934	0.09765	0.06217
0.25-0.3	0.00437	0.00792	0.01880	0.07791	0.20635	0.30079	0.21613	0.13928
0.3-0.35	0.00288	0.00613	0.01017	0.03177	0.09822	0.22540	0.33673	0.29702
0.35-0.4	0.00376	0.00460	0.00651	0.01542	0.04498	0.11951	0.25619	0.40982

Table B.3: The unfolding matrix for π^+ binned in x.

x	0.0-0.05	0.05-0.1	0.1-0.15	0.15-0.2	0.2-0.25	0.25-0.3	0.3-0.35	0.35-0.4
0.0-0.05	0.54435	0.13245	0.02992	0.01177	0.00431	0.00198	0.00131	0.00104
0.05-0.1	0.37728	0.55744	0.20930	0.06565	0.02889	0.01135	0.00572	0.00271
0.1-0.15	0.03375	0.22803	0.43327	0.21366	0.07921	0.03750	0.02193	0.01202
0.15-0.2	0.01436	0.04264	0.21861	0.35276	0.20018	0.08395	0.04336	0.03613
0.2-0.25	0.01262	0.01631	0.06548	0.21325	0.30902	0.19774	0.09163	0.06007
0.25-0.3	0.00748	0.00989	0.02309	0.08755	0.22035	0.30644	0.22339	0.13579
0.3-0.35	0.00407	0.00734	0.01219	0.03729	0.10512	0.23512	0.34520	0.32616
0.35-0.4	0.00609	0.00589	0.00815	0.01807	0.05292	0.12592	0.26746	0.42608

Table B.4: The unfolding matrix for π^- binned in x.

B.2 Correlation of x and z with track p_T

In the fits for background subtraction, every bin in x or z required a fit in each momentum bin as well. This is because the analysis variables are not perfectly correlated with track momentum. Figures B-1 and B-2 are histograms showing the the correlations of these variables with p_T. One can observe that z is almost a dimensionless stand-in for p_T, while x is independent of p_T.

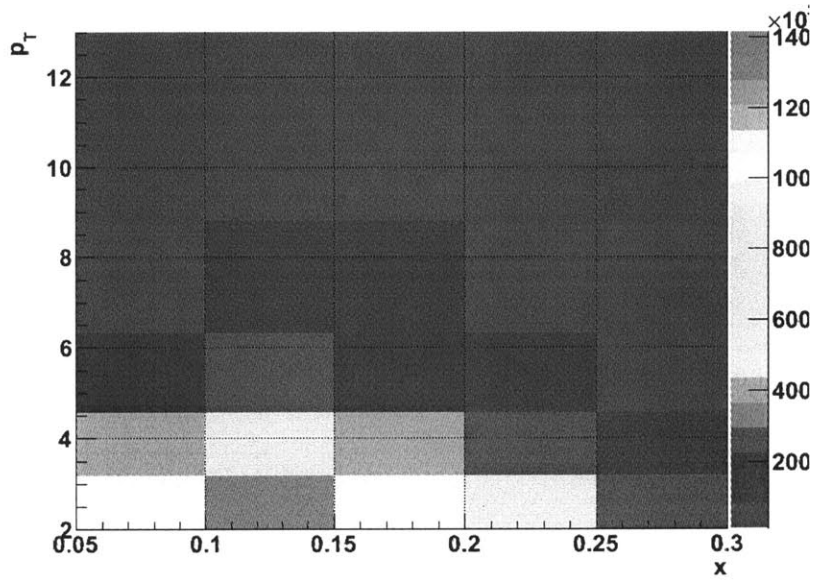

Figure B-1: Total track distribution in x and p_T.

B.3 Ratio of yields binned in z.

The idea of 'favored fragmentation' describes how a high-z pion likely contains a quark from the hard scattering interaction. Figure B-3 shows ratio of π^+ yield to π^- yield binned in z. The ratio increases from unity at low z up to almost two at high z. This can be viewed as representing a scale which moves from probing sea quarks (equal parts up and down) to the valence quarks (two ups to one down).

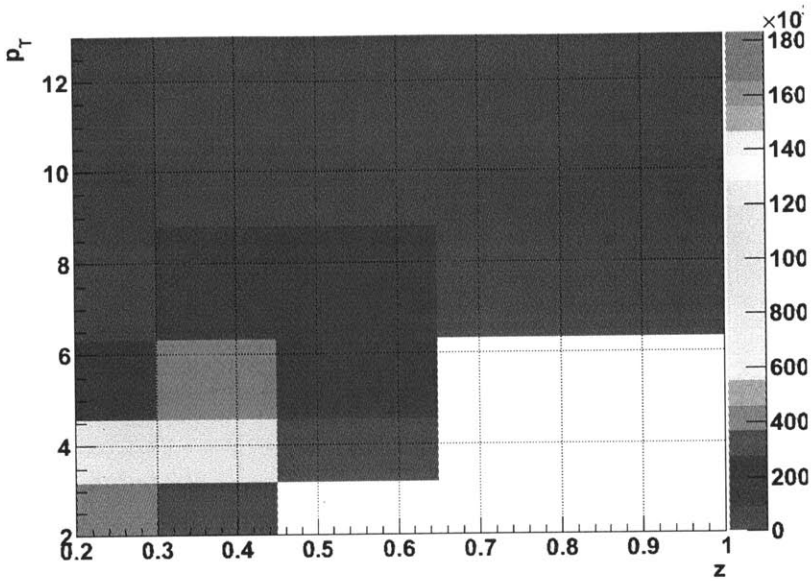

Figure B-2: Total track distribution in z and p_T.

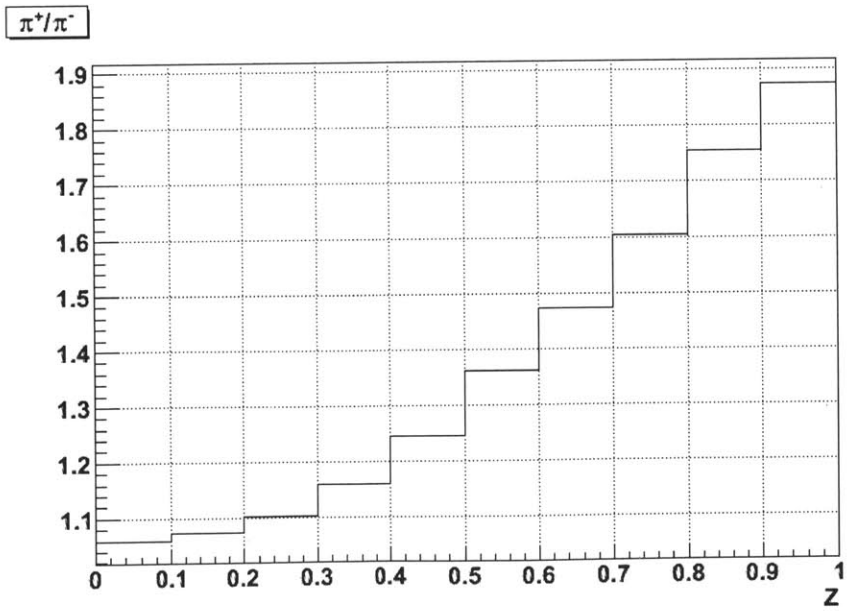

Figure B-3: The excess of positive pions compared to negative pions increases with z.

Bibliography

[1] R. Frisch and O. Stern. *Zeitschrift für Physik*, 85(4), 1933.

[2] W.M. Yao *et al.* Review of Particle Physics. *Journal of Physics G*, 33:1+, 2006.

[3] E. D. Bloom, D. H. Coward, H. DeStaebler, J. Drees, G. Miller, L. W. Mo, R. E. Taylor, M. Breidenbach, J. I. Friedman, G. C. Hartmann, and H. W. Kendall. High-energy inelastic $e-p$ scattering at 6° and 10°. *Phys. Rev. Lett.*, 23:930–934, Oct 1969.

[4] Wouter Verkerke. Phd thesis, 1999. nikhef.nl/pub/experiments/zeus/theses/wouter_verkerke/latex2html/img123.gif.

[5] Francis Halzen and Alan Martin. *Quarks & Leptons: An introductory course in modern particle physics.* John Wiley & Sons, New York, USA, 1984.

[6] V. E. Barnes *et al.* Observation of a Hyperon with Strangeness Minus Three. *Physical Review Letters*, 12:204–206, February 1964.

[7] John Ellis and Robert Jaffe. Sum rule for deep-inelastic electroproduction from polarized protons. *Phys. Rev. D*, 9:1444–1446, Mar 1974.

[8] J. Ashman et al. A Measurement of the Spin Asymmetry and Determination of the Structure Function g_1 in Deep Inelastic Muon-Proton Scattering. *Phys.Lett.*, B206:364, 1988.

[9] Daniel de Florian, Rodolfo Sassot, Marco Stratmann, and Werner Vogelsang. Global Analysis of Helicity Parton Densities and Their Uncertainties. *Phys.Rev.Lett.*, 101:072001, 2008.

[10] D. de Florian. Next-to-leading order QCD corrections to hadron+jet production in pp collisions at RHIC. *Phys. Rev. D*, 79(11):114014, June 2009.

[11] D. de Florian, R. Sassot, M. Stratmann, and W. Vogelsang. QCD spin physics: Partonic spin structure of the nucleon. *Prog.Part.Nucl.Phys.*, 67:251–259, 2012.

[12] M. Gluck, E. Reya, M. Stratmann, and W. Vogelsang. Models for the polarized parton distributions of the nucleon. *Phys. Rev.D*, 63:094005, 2001.

[13] William Leight. *Neutral Pion Double Helicity Asymmetry in Polarized Proton-Proton Collisions at $\sqrt{s} = 200$ GeV at STAR.* PhD thesis, Massachusetts Institute of Technology, Department of Physics, 2012.

[14] G. Hanson et al. Evidence for Jet Structure in Hadron Production by $e^+e^?$ Annihilation. *Phys. Rev. Lett.*, 35(1609), 1975.

[15] B. H. Wiik. First Results From Petra. volume 1, Bergen, 1979.

[16] T. Roser et al. First Polarized Proton Collisions at RHIC. www.rhichome.bnl.gov/RHIC/Runs/RhicProjections.pdf.

[17] A.N. Zelenski et al. Optically-pumped polarized H ion sources for RHIC and HERA colliders. *Proceedings of PAC 1999*, page 106, 1999.

[18] S. Diane Reitzner. *A Study and Optimization of Helicity-Correlated Beam Properties Generated from the TRIUMF Optically Pumped Ion Source for the Parity Violation Experiment at 221 MeV.* Master's thesis, University of Manitoba, Physics Department, June 1996.

[19] Thomas Roser. Spin rotators and split siberian snakes. *Nuclear Instruments and Methods in Physics Research Section A: Accelerators, Spectrometers, Detectors and Associated Equipment*, 342:343347, March 1994.

[20] Jeff Wood. *Polarimetry at the Brookhaven AGS Using Proton-Carbon Coulomb-Nuclear Interference.* PhD thesis, UCLA, 2005.

[21] M. Anderson et al. The STAR Time Projection Chamber: A Unique Tool for Studying High Multiplicity Events at RHIC. *Nuclear Instruments and Methods in Physics Research A*, 499:659–678, 2003.

[22] M. Beddo et al. The STAR Barrel Electromagnetic Calorimeter. *Nuclear Instruments and Methods in Physics Research A*, 499:659–678, 2003.

[23] J. Kiryluk. volume 675 of *AIP Conf. Proc.*, page 424, 2003.

[24] C. Adler et al. *Nuclear Instruments and Methods in Physics Research A*, 470:488–499, 2001.

[25] R. Reed et al. Vertex finding in pile-up rich events for p+p and d+au collisions at star. *Journal of Physics: Conference Series*, 219(3):032020, 2010.

[26] G. C. Blazey *et al.* Run II jet physics. hep-ex/0005012.

[27] Adam Kocoloski. *Measurement of Longitudinal Double Spin Asymmetries of $\pi^{\pm}$ Production in p+p Collisions at $\sqrt{s} = 200$ GeV at RHIC.* PhD thesis, Massachusetts Institute of Technology, 2010.

[28] J. Sowinski. Star internal communication. http://www.star.bnl.gov/protected/spin/sowinski /analysis/derivations/multiParticle.pdf.

[29] Torbjorn Sjostrand, Stephen Mrenna, and Peter Skands. Pythia 6.4 physics and manual. *JHEP*, 05(026), 2006.

[30] T. Sjöstrand. The lund monte carlo for jet fragmentation. *Computer Physics Communications*, 1982.

[31] Geant User's manual. http://geant4.cern.ch/support/userdocuments.shtml.

[32] Matthew Walker. *Dijet Production in Polarized Proton-Proton Collisions at* $\sqrt{s} = 200$ *GeV*. PhD thesis, Massachusetts Institute of Technology, Department of Physics, 2011.

[33] G. D'Agostini. A multidimensional unfolding method based on Bayes' theorem. *Nuclear Instruments and Methods in Physics Research A*, 362:487–498, 1995.

[34] D Cronin-Hennessy, A Beretvas, and PF Derwent. Luminosity monitoring and measurement at cdf. *Nuclear Instruments & Methods In Physics Research Section A-Accelerators Spectrometers Detectors and Associated Equipment*, 443(1):37–50, MAR 21 2000.

[35] J. Hays-Wehle, J. Seele, H. Spinka, and B.Surrow. Relative Luminosity Analysis for run9 pp 200 GeV Running. *STAR Note*, 570. http://drupal.star.bnl.gov/STAR/starnotes/private/psn0570.

[36] RHIC CNI Polarimeter Group. http://www4.rcf.bnl.gov/ cnipol/pubdocs/Run09Offline/.

[37] Pibero Djawotho. Gluon polarization measurements with inclusive jets at STAR. 2011. nucl-ex:1106.5769.